JOURNAL OF PROPULSION AND POWER
Vol. 22, No. 5, September–October 2006

# Liquid Metal Loop and Heat Pipe Radiator for Space Reactor Power Systems

Jean-Michel P. Tournier* and Mohamed S. El-Genk†
*Institute for Space and Nuclear Power Studies, University of New Mexico, Albuquerque, New Mexico 87131*

DOI: 10.2514/1.20031

**This paper presents four radiator configurations that could be stowed in the launch bay of the DELTA-IV Heavy vehicle and have effective areas of 69.1 to 350 $m^2$. The radiator for a space reactor power system with a lithium-cooled sectored compact reactor and thermoelectric converters has an effective area of 203 $m^2$ and lowest specific mass. The sectored compact reactor and thermoelectric converters system generates ~114 kWe for 7–10 years. The radiator consists of six panels, each having a forward, fixed segment and two rear, deployable segments, and rejects heat into space using rubidium heat pipes with carbon–carbon armor and fins. The D-shaped heat pipes operate below 50% of the prevailing sonic or capillary limit. The radiator operates at a constant pressure drop of 12 kPa and inlet and exit temperatures of 780 and 755 K. Investigated are the effects on the radiator's specific mass and lithium inventory of 1) tapering and changing width of coolant channels, 2) thermal-hydraulically coupling the panel segments in parallel, and 3) using perforated dividers between inlet- and exit-channels. The radiator with perforated dividers has a wet specific mass of 6.82 $kg/m^2$, a liquid-lithium inventory of 179.3 liters, and a stowed height of 8 m.**

## Nomenclature

| | | |
|---|---|---|
| $A$ | = | surface area, or flow cross section area, $m^2$ |
| $C_p$ | = | coolant specific heat capacity, $J/kg \cdot K$ |
| $D$ | = | equivalent diameter of flow channel, m |
| $D_V$ | = | diameter of heat pipe vapor space, m |
| $d_{orif}$ | = | circular orifices diameter, m |
| $F$ | = | local radiation view factor |
| $f$ | = | Darcy friction coefficient, $f = a/Re^b$ |
| $H$ | = | height, height of flow channel, m |
| $H_V$ | = | height of D-shaped, heat pipe vapor space, m |
| $h_{fg}$ | = | latent heat of vaporization, J/kg |
| $\bar{h}^{fin}$ | = | fin average heat transfer coefficient, $W/m^2 \cdot K$ |
| $h^*$ | = | dimensionless, fin heat transfer coefficient |
| $K$ | = | dimensionless pressure loss coefficient |
| $\bar{k}^{fin}$ | = | fin average thermal conductivity, $W/m \cdot K$ |
| $L$ | = | length of radiator panel segment, m |
| $L_{cd}$ | = | heat pipe condenser length, m |
| $L_{ev}$ | = | heat pipe evaporator length, m |
| $L_i$ | = | section length for computing $\Delta P$, m |
| $\dot{M}_i$ | = | crossflow rate through orifices, kg/s |
| $M_L$ | = | figure-of-merit, $W/m^2$ |
| $\dot{m}_i$ | = | axial mass flow rate along channel, kg/s |
| $N$ | = | number of axial sections along radiator segment |
| $N''$ | = | orifices number density, # per $m^2$ |
| $n_{HP}$ | = | number of heat pipes in radiator segment |
| $Q$ | = | radiative heat rejection to space, $W_{th}$ |
| $R$ | = | radius, m |
| $Re$ | = | flow Reynolds number, $Re = \rho_L \bar{V} D/\mu$ |
| $T$ | = | temperature, K |
| $\bar{T}^{fin}$ | = | average carbon–carbon fin temperature, K |
| $T_{sink}$ | = | space sink temperature, K |
| $\bar{V}$ | = | average flow velocity, m/s |
| $W$ | = | width of coolant channel, m |
| $W_{fin}$ | = | width of carbon–carbon fin, m |
| $\alpha$ | = | aspect ratio of D-shaped heat pipe, $\alpha = H_V/D_V$ |
| $\beta$ | = | orifices area ratio, $\beta = A^{orif}/(H\Delta Z)$ |
| $\delta$ | = | thickness, m |
| $\Delta P$ | = | pressure drop, Pa |
| $\Delta T$ | = | coolant temperature drop through radiator, K |
| $\Delta Z$ | = | length of each axial section, $\Delta Z = L/N$, m |
| $\varepsilon$ | = | wick volume porosity, radiative emissivity |
| $\varepsilon^o$ | = | orifices pressure loss correction factor |
| $\eta^{fin}$ | = | thermal efficiency of carbon–carbon fin |
| $\mu$ | = | liquid dynamic viscosity, $kg/m \cdot s$ |
| $\rho$ | = | density, $kg/m^3$ |
| $\sigma$ | = | Stefan–Boltzmann constant, $\sigma = 5.67 \times 10^{-8}$, $W/m^2 \cdot K^4$ |
| $\sigma_L$ | = | liquid surface tension, N/m |
| $\Phi^{vis}$ | = | coolant viscous dissipation, W |

*Subscripts/Superscripts*

| | | |
|---|---|---|
| $b$ | = | coolant bulk temperature |
| base | = | base of carbon–carbon fin |
| $C$ | = | coolant exit-channel |
| cd | = | heat pipe condenser |
| dis | = | orifices discharge |
| ev | = | heat pipe evaporator |
| ex | = | coolant at exit of radiator segment channel |
| fin | = | carbon–carbon fin |
| gap | = | liquid-return annulus in heat pipe |
| $H$ | = | coolant inlet-channel |
| HP | = | heat pipe |
| in | = | coolant at inlet of radiator segment channel |
| $L$ | = | liquid phase of heat pipe working fluid |
| liner | = | metallic liner/wall of heat pipe, Ti |
| orif | = | orifices in divider wall |
| rad | = | radiator panel |
| turb | = | turbulent flow |

Received 12 September 2005; revision received 24 January 2006; accepted for publication 28 January 2006. 

*Research Assistant Professor, Chemical and Nuclear Engineering Department, Institute for Space and Nuclear Power Studies.

†Regents' Professor of Chemical and Nuclear Engineering and Director, Institute for Space and Nuclear Power Studies; (505) 277-5442; Fax: (505) 277-2814; mgenk@unm.edu.

| | | |
|---|---|---|
| $V$ | = | heat pipe vapor space |
| $w$ | = | outer carbon–carbon armor of heat pipe |
| wick | = | porous wick of heat pipe, Ti |

## Introduction

POWER requirements for future planetary orbital and surface missions range from 10s to 1000s of kilowatts electric kWe for up to 15 years. For these missions, nuclear reactor power systems (NRPSs) are an excellent option because of the limited solar option on Mars and its absence on other farther planets such as Jupiter, Saturn, Neptune, and Pluto. NRPSs are compact and have low alpha of ~25–50 kg/kWe compared with 100–200 kg/kWe for radioisotope power systems (RPSs) [1]. The type of space reactors (hard–fast, soft–fast, or thermal neutron spectrum) and operation temperatures (1000–1500 K), and the type of energy conversion technology (static or dynamic) dictate the total size and mass of the NRPS. They also determine the choices of structural materials and launch vehicle, and define the design and operation requirements of the heat rejection radiator, and hence the total mass, effective surface areas, and design of radiator. The radiator is typically the heaviest and largest system component. Therefore, early consideration is given to the design and optimization of the radiator and its packaging into the bay of the launch vehicle of choice. The DELTA-IV Heavy vehicle is considered in the present analysis for launching the sectored compact reactor and thermoelectric converters (SCoRe-TE) NRPS.

A 500 kWe NRPS with sodium alkali metal thermal-to-electrical converters (AMTEC) [2] or a potassium Rankine cycle (PRC) [3] rejects waste heat into space at average radiator surface temperatures of 650–800 K. At such surface temperatures, the radiator is relatively small, with an effective heat rejection area ~200 m$^2$ and employs liquid-metal heat pipes with carbon carbon (C–C) armor and fins. By contrast, for the same electrical power when using recuperated-closed Brayton cycle (CBC) [4,5] engines or free piston Stirling engines (FPSEs) [6], the waste heat is rejected into space at much lower temperatures of 400–450 K. At these temperatures, water heat pipe radiators could be used with an effective area that is ~3 times larger (~600 m$^2$). In addition to being heavy, such large radiators are a challenge to stow in the bay of the launch vehicle and to deploy.

Heat pipe radiators are preferred because of their inherent redundancy and efficient spreading and rejection of waste heat into space at a relatively small mass penalty. The coolant type (gas or liquid metal) and the cold temperature of the selected energy conversion technology option dictate the radiator's effective surface temperature and the design and working fluid of the radiator heat pipes, and hence, the radiator's specific mass. For radiator surface temperatures of 600–800 K, choices of heat pipe working fluid with increasing temperature are cesium, rubidium, and potassium. Water is only suitable for radiator temperatures of 300–500 K [7].

This paper develops four configurations of a rubidium heat pipe radiator that could be stowed in the launch bay of the DELTA-IV Heavy vehicle and used in an NRPS with a sectored compact reactor (SCoRe) and SiGe thermoelectric (TE) power conversion assemblies (PCAs). The PCAs nominally operate at hot and cold side temperatures of 1150 and 800 K [8]. The selected radiator configuration for SCoRe-TE NRPS is for nominally generating >110 kWe for 7–10 years [8,9] and has the lowest specific mass. This radiator design is optimized for operating at constant pressure losses of 12 kPa and inlet and exit temperatures of 780 and 755 K. Investigated are the effects on the radiator's specific mass and liquid-lithium inventory in the radiator's channels of 1) tapering the coolant channels in the forward and rear segments, 2) changing the width of the coolant channels, 3) thermal-hydraulically coupling the three segments in each of the six radiator panels in parallel, and 4) using perforated dividers between the lithium inlet- and exit-channels. The number density of the 1.0 mm diam orifices in the dividers is optimized for maintaining almost uniform, but different temperatures in the inlet and exit coolant channels of the radiator segments.

## Integration of SCoRe-TE NRPS into DELTA-IV Heavy

The DELTA-IV Heavy launch vehicle has a payload fairing diameter of 4.57 m and a stowed height of 15.71 m (Figs. 1a–1c). It could place 6276 kg into a geosynchronous earth orbit (GEO), and 8005 kg into a C3 insertion orbit to Mars [10]. The NRPS could be stowed in a single-manifest vehicle configuration (Fig. 1a), or in the upper compartment of a dual-manifest vehicle for a reduced launch cost (Figs. 1b and 1c). In this launch option, an additional payload is loaded in the lower compartment to ensure center-of-gravity and payload/launch vehicle interface and vibration compliance. Although these are critical issues that should be addressed earlier in the development process, they are outside of the scope of this work. The NRPS is launched with the nuclear reactor at the nose of the rocket, followed immediately by the radiation shadow shield, and then the stowed radiator. The cone angle for the SCoRe-TE NRPS is 30 deg and the minor diameter of the radiator is 1.08 m. When fully deployed in orbit (Figs. 2a–2d), the shadow shield protects the system components and payload behind it from the fast neutrons and high-energy gamma rays of the nuclear reactor [8,9]. Figure 2 shows the four radiator configurations developed in this study for potential integration into the SCoRe-TE NRPS. The selected radiator for subsequent system analysis is based on satisfying the following requirements: 1) the stowed NRPS fits into the launch bay of the DELTA-IV Heavy vehicle; 2) the SCoRe-TE NRPS nominally generates at least 110 kWe [8,9]; and 3) the radiator's specific mass <7.5 kg/m$^2$.

In Fig. 2, the geometrical and effective areas of the radiator are listed in the caption below each configuration, and $A_i$ and $F_i$ indicate the geometrical areas of the radiator panel segments and their effective radiation view factors, respectively. The radiator configuration-A (Fig. 2a) is composed of six fixed panels whose extent is limited by the inner diameter (4.57 m) of the payload fairing. Consequently, the total height of this radiator is 6.53 m and each panel has a geometrical area $A_1 = 9.46$ m$^2$ and effective radiation view factor $F_1 = 1.218$. This view factor accounts for the thermal radiation from the outer surface as well as from the inner surface through the rear opening of the radiator cavity. The calculated effective radiation view factor of the inner surface assumes 20% obstruction by the payload boom and other equipment placed within the radiator cavity. This radiator with a total effective heat rejection area and geometrical area of 69.1 and 56.7 m$^2$, respectively, and a stowed height of only 8.03 m, fits in the upper compartment of a dual-manifest vehicle arrangement (Figs. 1b and 1c). Because of the small surface area, this radiator is excluded; it is only suitable for low power generation (<50 kWe).

The radiator configuration-B has six forward, fixed segments, similar to the panels in configuration-A, and 12 rear, deployable segments (Fig. 2b) similar to those of the SP-100 system [11]. Thus,

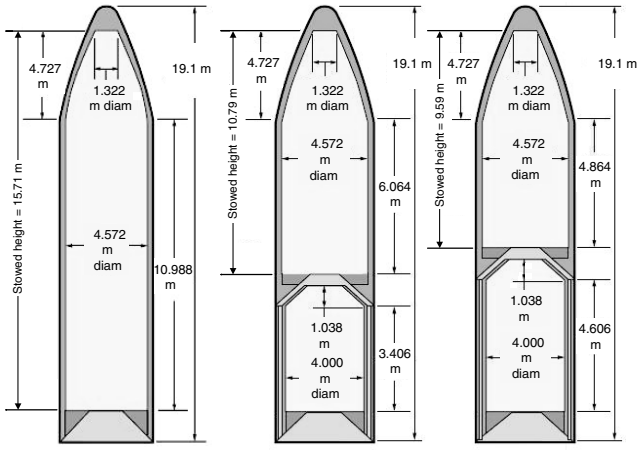


**a) Existing capability (single manifest)** **b) Growth option A (dual manifest)** **c) Growth option B (dual manifest)**

**Fig. 1 Fairing envelopes of DELTA-IV Heavy launch vehicle [10].**

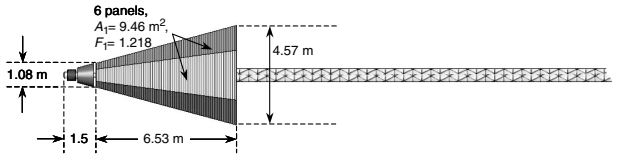


**a) Fixed radiator design configuration–A, 56.8 m$^2$, 69.1 m$^2$**

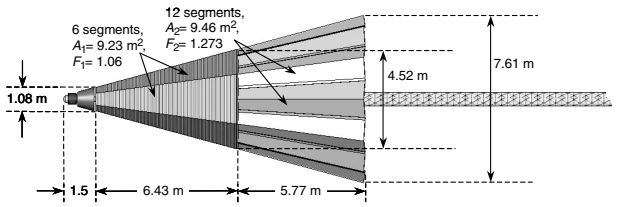


**b) Deployable radiator design configuration–B, 168.9 m$^2$, 203 m$^2$**

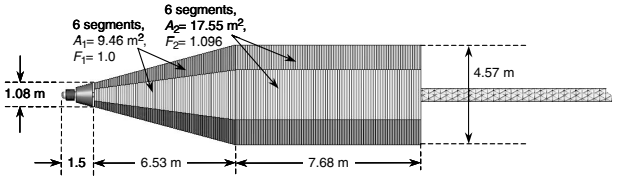


**c) Fixed radiator design configuration–C, 162.1 m$^2$, 172 m$^2$**

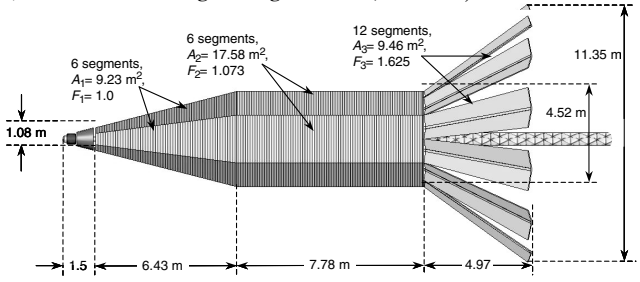


**d) Deployable radiator design configuration–D, 274.4 m$^2$, 353 m$^2$**

**Fig. 2 Radiator configurations developed for the DELTA-IV Heavy launch vehicle.**

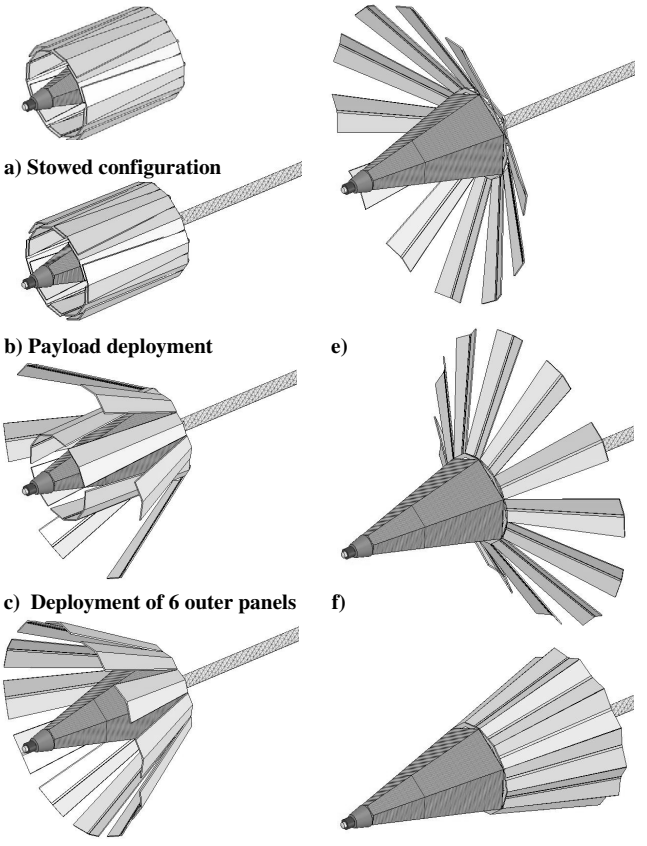


**Fig. 3 Deployment sequence of SCoRe-TE NRPS.**

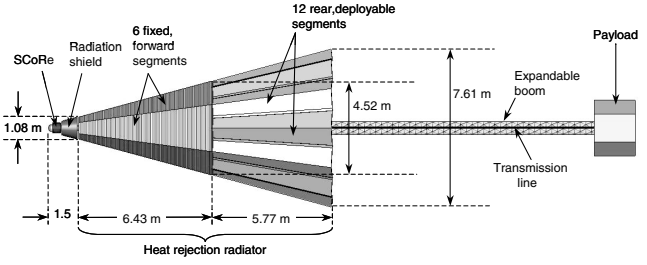


**Fig. 4 Layout of SCoRe-TE NRPS.**

each of the six radiator panels consists of a forward, fixed segment and two rear, deployable segments. The stowed configuration and deployment sequence of this radiator, whose performance and mass estimates are discussed later in the paper, are shown in Fig. 3. In the stowed configuration, six of the 12 rear deployable segments are folded over the six forward fixed segments. The other six rear deployable segments, when folded, overlap the first six folded segments (Fig. 3a). The height of the forward fixed segment of the radiator panel (6.43 m) is limited by the diameter of the payload fairing. With 2.7-cm-thick heat pipes, the thickness of the deployable segments is 3.9 cm, which decreases the major diameter of the fixed segment of the radiator panels to 4.52 m (Figs. 2b and 4), resulting in a geometrical area $A_1$ of 9.23 m$^2$.

When deployed, the inside surfaces of the fixed segments of the panels of this radiator are obstructed partially by the rear segments and thus, their effective radiation view factor $F_1$ decreases to only 1.06. The extent (5.77 m) of the deployed rear segments is limited by their overlap in the stowed configuration (Fig. 3a), hence dictating the radiator major diameter (7.61 m). Each rear segment has a geometrical area, $A_2 = 9.46$ m$^2$, and a larger, effective radiation view factor, $F_2 = 1.273$. As a result, the effective heat rejection area of this radiator (Fig. 2b) of 203 m$^2$ is nearly three times that of configuration-A (Fig. 2a) for an identical stowed volume. It has a specific mass $<7.1$ kg/m$^2$, satisfying the down selection requirements stated earlier, and thus selected for the SCoRe-TE NRPS analyzed in this work.

The radiator configurations-C and D take advantage of the long fairing (15.71 m) of the DELTA-IV Heavy launch vehicle with the single-manifest (Fig. 1a). Configuration-C consists of six fixed, forward segments, which are identical to those in configuration-A, and six rear fixed rectangular segments that are 7.68 m long (Fig. 2c) and have a major diameter of 4.57 m. This radiator is 15.71 m long and has a geometrical area of 162.1 m$^2$, but because of the small radiation view factors ($F_1 = 1.0$ and $F_2 = 1.096$), it has an effective area of only 172 m$^2$, which is smaller than that of configuration-B (Figs. 2b and 2c). Even though the geometrical surface area of this radiator is only 4% smaller than configuration-B (168.9 m$^2$), its effective heat rejection area is 15% smaller. Thus, configuration-C is excluded from further consideration because of the small effective area, which translates into lower system electric power and larger volume and mass, increasing the launch cost.

Configuration-D is an improvement on configuration-C, adding 12 rear deployable segments to an angle of 34.6 deg, while remaining within the shadow of the radiation shield (Fig. 2d). The major diameter of the deployed panels is 11.35 m and their effective radiation view factor is 1.625. Configuration-D has effective and geometrical areas of 353 and 274.4 m$^2$, respectively, which are 74% and 62% higher than those of configuration-B. Although the radiator configuration-D is suitable for a 200 kWe class SCoRe-TE power system, it is much heavier than configuration-B for the system requirements stated earlier. The large deployed length and the higher mass of the support structure and the coolant channels in configuration-D increase its specific mass ($>9$ kg/m$^2$), beyond that stated in the down selection requirements ($<7.5$ kg/m$^2$).

Figures 3a and 3b show the SCoRe-TE NRPS with the radiator configuration-B in the stowed configuration, before and after the payload boom is erected. Figures 3c–3g show the sequences of deploying the 12 rear segments of the heat pipe radiator. Figure 3a is identical to Fig. 4, showing the fully deployed SCoRe-TE NRPS. Note that the fixed segments and the rear deployable segments of the radiator panels are connected using flexible piping joints. Upon full deployment of the SCoRe-TE NRPS, the startup procedure of the nuclear reactor begins, while disconnecting the electrical load [8,9]. The load is connected after the reactor reaches steady state at the end of the startup procedure. Connecting the electrical load subjects the system to a short transient followed by steady-state operation at nominal conditions, at which the electrical load power is ~114 kWe [8].

## Sectored Compact Reactor

The lithium-cooled SCoRe [12] used in the present NRPS is divided into six identical, hydraulically-independent, but neutronically coupled sectors (Figs. 5a and 5b). Each reactor sector has its own primary coolant and a secondary loop with a separate radiator panel (Fig. 4). This arrangement provides redundancy in the reactor liquid metal (LM) cooling and system integration for avoidance of a single point failure. The reactor consists of a hexagonal core surrounded by a relatively thick (>10 cm) BeO radial reflector and 4-cm-thick BeO axial reflectors (Figs. 5a and 5b). A total of six BeO rotating control drums with thin (>5 mm) $B_4C$ segments are inserted in the radial reflector to start up the reactor and regulate its thermal power. In the shutdown mode, the $B_4C$ segments face the reactor core, and face away at the end of the operation life of the reactor.

The SCoRe core sectors are loaded with UN fuel pins with Mo-14Re cladding [12]. The cladding has a wire wrap of the same material on the outside surface to maintain uniform flow channels and provide structural integrity of the assembled reactor core (Fig. 5c). The lithium returning to a core sector flows upward in an annulus on the inside of the reactor vessel wall, then reverses direction at the opposite end (Fig. 5c) to flow through the sector and remove the heat generated by fission in the UN fuel pins. The liquid lithium exits the reactor core from the lower plenum (Fig. 5c). The sectors in the SCoRe are physically separated using liquid-metal heat pipe dividers (Fig. 5b). These dividers passively cool the reactor sector experiencing a loss of coolant. They transport the fission power generated in that sector to the circulating lithium in the adjacent sectors [12]. Figure 5b shows a radial cross section of SCoRe, in which each sector is loaded with 171 fuel pins for a total of 1026 pins, and which nominally may generate up to 4 $MW_{th}$ for 7–10 years.

## SCoRe-TE NRPS

The SCoRe-TE NRPS (Fig. 4) uses SiGe [13] thermoelectric power conversion assemblies (PCAs) that are placed between the lithium primary and secondary loops. The PCAs, which are similar in design to those of the SP-100 space nuclear reactor power system [14,15], operate nominally at hot and cold side temperatures of 1150 and 800 K, have an efficiency of 4.3%, and deliver 114 kWe at 450 volts of direct current (Vdc), at a reactor exit temperature of only 1179 K (Fig. 6). The lithium coolant in the six primary and six secondary loops is circulated using 12 electromagnetic (EM) dc conduction pumps, one in each loop. The electrical current to each pair of a primary and a secondary pump is supplied by a dedicated TE conversion assembly (TCA), which is placed between the primary and secondary loops (Fig. 6). The liquid-lithium secondary loop transports the rejected heat from the PCA and the pumps' TCA to a rubidium heat pipe radiator panel. The six lithium primary loops transport the thermal power generated in the reactor sectors to the six PCAs and six pumps' TCAs. The PCAs have built-in redundancy using four parallel strings of SiGe unicouples. Each parallel string

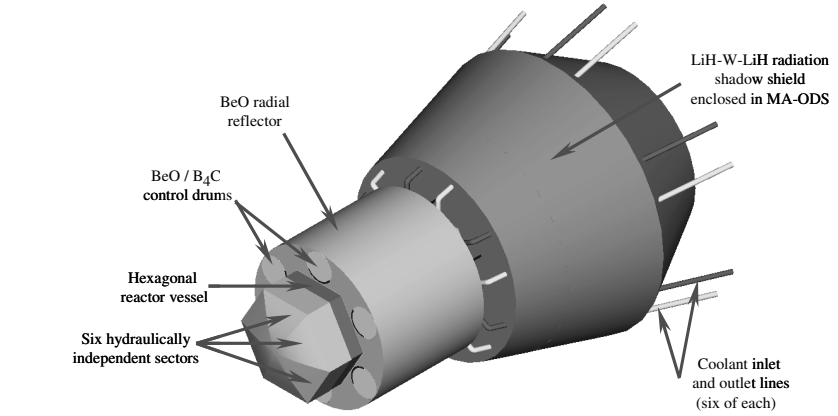


**a) Layout of SCoRe-$S_{11}$**

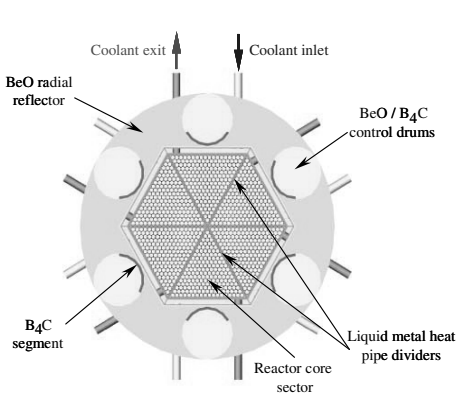


**b) Radial cross section**

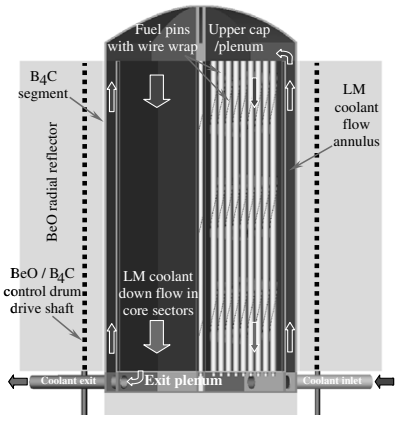


**c) Axial cross section and coolant flow**

**Fig. 5 Radial and axial cross sections of SCoRe-$S_{11}$ core (not to scale).**

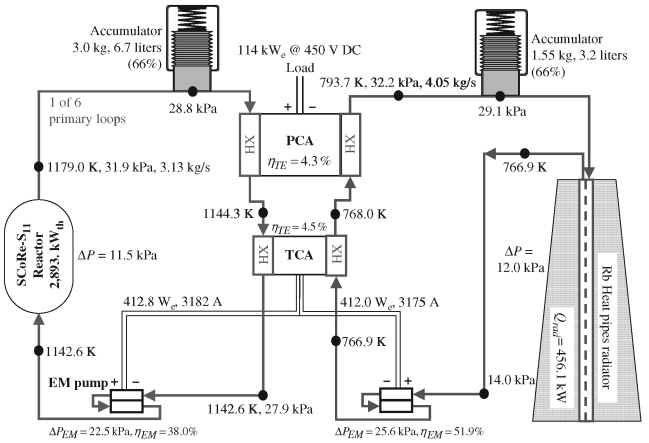


**Fig. 6 Nominal steady-state operation parameters of SCoRe-TE NRPS.**

consists of 5400 SiGe unicouples connected electrically in series. The PCAs, connected electrically in parallel for additional redundancy, operate at a steady-state, nominal load voltage of 450 Vdc for potential operation of ion thrusters as well as for reducing the joule losses in the power management and distribution. The SiGe unicouples in the TCA are connected electrically in parallel in two-series strings to provide the highest electrical current to the pumps. Each half TCA provides electrical power to a primary or a secondary EM Pump. The nominal electric current supplied to each pump is typically ~3200 amperes at ~130 mV.

The static PCAs and pumps' TCAs are inherently load following, which together with the negative reactivity feedback of SCoRe make the NRPS inherently load following, a major operation and reliability advantage. The nominal electrical power of SCoRe-TE is 114 kWe at a load voltage of 450 Vdc, and a net efficiency of 3.94% (Fig. 6). These parameters are attainable at a reactor power of 2.89 $MW_{th}$ and a relatively low reactor exit temperature of 1179 K. The design of the optimized heat pipe radiator used in the SCoRe-TE NRPS is described in details next.

## Heat Pipe Radiator Panel

As indicated in the preceding section, the selected radiator in Figs. 2b and 4 has six panels; each panel consists of a forward fixed segment and two rear, deployable segments (Fig. 7). The forward segment is 6.605 m long and has an effective surface area, $A_1 \times F_1 = 9.78$ m$^2$, whereas each rear segment is 5.952 m long and has a higher effective surface area, $A_2 \times F_2 = 12.04$ m$^2$ (Fig. 7a). Heat is removed from the circulating lithium coolant in the channels of the panels and rejected into space using rubidium heat pipes with C–C fins and armor. The heat pipes are placed perpendicular to the lithium flow in the inlet and exit coolant channels (Fig. 7). The C–C armor of the heat pipes protects them against meteoroid impact, and the C–C fins enhance the radiator heat rejection. As shown in Fig. 7a, the secondary lithium coolant exiting the PCA is fed to three coolant channels, one for each segment of the radiator panel. This parallel hydraulic connection decreases the cross section areas of the channels, and hence the mass and inventory of the lithium secondary coolant. Feeding the coolant in the forward segment at the end with the longest heat pipes also improves both the thermal and hydraulic performances of this segment, as will be shown later.

The longest and shortest heat pipes in the forward segment of the radiator panel are 1.13 and 0.268 m long, respectively, (Fig. 8a), whereas those in the rear, deployable segments are 1.0 and 0.59 m long, respectively, (Fig. 8b). The evaporator lengths of the heat pipes are equal to the underlying widths of the coolant channels. In the forward radiator segment, the width of the coolant channels is tapered linearly from 10 cm at the inlet/exit to 4 cm at the back end (Fig. 8a). As a result, the longest heat pipes near the inlet/exit have 10-cm-long evaporator sections, while the shortest ones have 4-cm-long evaporators. In contrast, the coolant channels of the rear radiator

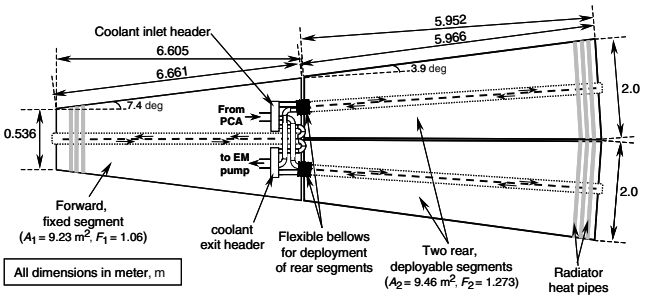


**a) Segmented radiator panel design**

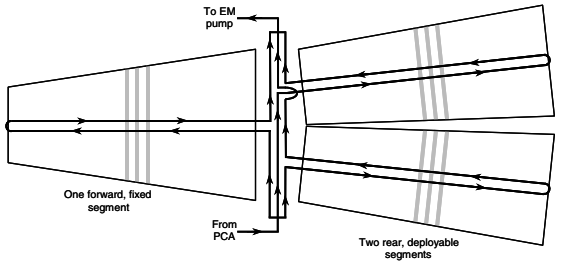


**b) Coolant flow through forward and rear segments of a radiator panel**

**Fig. 7 Design and layout of segmented radiator panel.**

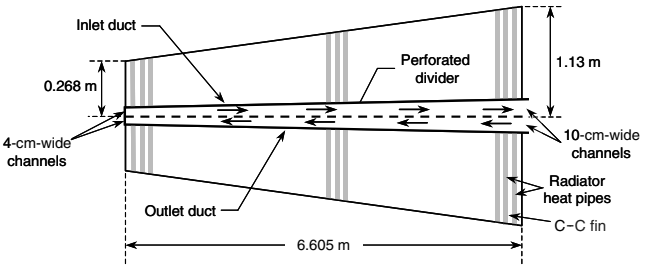


**a) Forward, fixed radiator panel segment (1 of 6)**

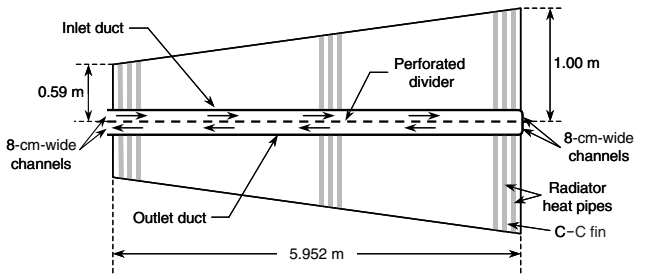


**b) Rear, deployable radiator panel segment (1 of 12)**

**Fig. 8 Layout of radiator panel segments with perforated dividers (not to scale).**

segments are rectangular (Fig. 8b) with a constant width of 8 cm, so that all the heat pipes have 8-cm-long evaporator sections. Each forward segment uses a total of 120 heat pipes, whereas each rear segment uses 144 heat pipes with connecting C–C fins that are 0.5 mm thick (Fig. 9). Results showed that increasing the fins thickness beyond 0.5 mm increases the radiator mass, while the heat rejection to space remains essentially unchanged.

The baseline radiator design selected in the preceding section capitalizes on the excellent progress made in radiator design [11,14] and the demonstrated operation and lifetime of liquid-metal heat pipes during the SP-100 program in the 1980s and early 1990s. Most heat pipe testing at Los Alamos National Laboratory has been with lithium, sodium, and potassium working fluids. In the present radiator design, however, rubidium heat pipes are selected, for which existing database is limited, thus lifetime testing is needed in

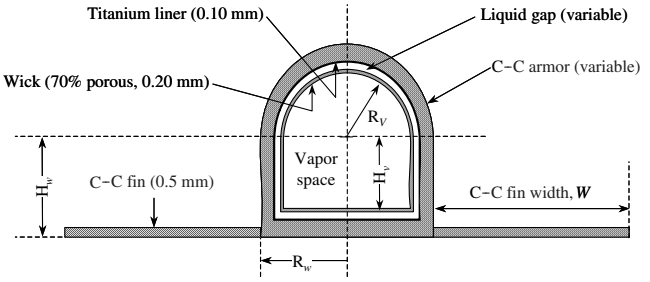


**Fig. 9 Radiator heat pipe with C–C armor and fins.**

the temperature range of interest in the SCoRe-TE NRPS (700–780 K). Rubidium has a higher vapor pressure than potassium, reducing the cross section area of the heat pipe and the radiator mass at the same vapor Mach number. Its vapor pressure is nearly identical to that of cesium, but its figure-of-merit (FOM) is 60% higher, resulting in a thinner heat pipe wick/liquid annulus and lower heat pipe mass when transporting the same power throughput. In addition, the density of liquid rubidium (1300 kg/m$^3$) is 20% lower than that of liquid cesium (1610 kg/m$^3$), further reducing the mass of the heat pipes.

Material compatibility tests involving the rubidium working fluid with titanium liner and wall at 700–800 K for extended periods are needed. The C–C armor and wall of the rubidium heat pipes in the baseline radiator design (Fig. 9) was developed and demonstrated successfully in the SP-100 program [11]. Carbon–carbon heat pipes with integral fins were successfully manufactured using a T-300 fiber, an angle interlocking weave architecture, and pitch densification. The fabricated C–C shells had a diameter of 2.54 cm and a wall thickness of 0.864 mm, with a C–C bulk density of 1650 kg/m$^3$ [11]. Since then, much progress has been made in the manufacturing of C–C fibers and composites, providing more flexibility in designing C–C shells of proper strength and thermal conductance in the circumferential and radial directions.

## Radiator Rubidium Heat Pipes

As shown in Fig. 9, the rubidium heat pipes for the radiator are D-shaped, with a semicircle radius $R_V$ and a rectangular section that is $H_V$ high. The flat side provides good integration and thermal coupling to the underlying coolant channels. The 0.2-mm-thick titanium (Ti) wick consists of three layers of 150-mesh screen with an average pore radius of 50 $\mu$m and effective volume porosity of 0.70 (Table 1). To decrease the pressure losses of the rubidium liquid returning from the condenser to the evaporator section, hence raising the capillary limit, the wick is separated from the 0.1-mm-thick Ti wall by a ~0.4-mm-thick liquid annulus (Fig. 9). The heat pipes are protected against meteorite impact by ~1.8-mm-thick C–C armor and have 0.5-mm-thick C–C fins. The thickness of the C–C armor is a function of the exposed surface area to space, and thus varies with the length of the heat pipes. The cross section flow area of the vapor, which is the same in all heat pipes, is selected such that the longest heat pipes operate at no more than 50% of the sonic limit. Also, the thickness of the liquid annulus is sized such that the longest heat pipes operate at no more than 50% of the capillary limit. These design choices ensure that all heat pipes in the radiator operate at < 50% of the prevailing sonic and/or capillary limits, and provide excellent redundancy since a failure of one or more heat pipes could be accommodated by adjacent heat pipes without exceeding any of the operation limits.

### Geometry Optimization

For a given flow area and aspect ratio, the radius and height of the vapor space in a heat pipe can be calculated as

$$R_V = [A_V/(\pi/2 + 4\alpha)]^{0.5} \quad \text{and} \quad H_V = 2\alpha R_V \tag{1}$$

The outer radius and height of the wick are then given by

$$R_{\text{wick}} = R_V + \delta_{\text{wick}} \quad \text{and} \quad H_{\text{wick}} = H_V + \delta_{\text{wick}} \tag{2}$$

The thickness of the liquid annulus is also calculated as

$$\delta_{\text{gap}} = \left(\sqrt{U^2 + (8 + 2\pi)A_{\text{gap}}} - U\right) \Big/ (4 + \pi)\delta \tag{3a}$$

where

$$U = (2 + \pi)R_{\text{wick}} + 2H_{\text{wick}} \tag{3b}$$

The outer radius and height of the liquid annulus are given as

$$R_{\text{gap}} = R_{\text{wick}} + \delta_{\text{gap}} \quad \text{and} \quad H_{\text{gap}} = H_{\text{wick}} + \delta_{\text{gap}} \tag{4}$$

and those of the titanium liner and of the surrounding C–C armor can be expressed, respectively, as

$$R_{\text{liner}} = R_{\text{gap}} + \delta_{\text{liner}} \quad \text{and} \quad H_{\text{liner}} = H_{\text{gap}} + \delta_{\text{liner}} \tag{5}$$

and

$$R_w = R_{\text{liner}} + \delta_w \quad \text{and} \quad H_w = H_{\text{liner}} + \delta_w \tag{6}$$

The thickness of the C–C armor $d_w$, however, is a function of the exposed surface area of the heat pipe to space ($A_{\text{exp}} = (L_{\text{ev}} + L_{\text{cd}}) \times \text{MAX}\{H_w + R_w, 2R_w\}$), and thus, it is necessary to iterate to obtain $\delta_w$.

The overall cross-sectional area of the heat pipe is then given as

$$A_{\text{HP}} = (\pi R_w/2 + 2H_w) \times R_w \tag{7}$$

The cross-sectional areas of the different zones of the heat pipe ($A_{\text{wick}}$, $A_{\text{gap}}$, $A_{\text{liner}}$, and $A_w$) are calculated and used to determine the mass of the heat pipe per unit length (kg/m), $\hat{\rho}_{\text{HP}}$, as

$$\hat{\rho}_{\text{HP}} = \rho_w A_w + \rho_{\text{Ti}} \times [A_{\text{liner}} + (1 - \varepsilon)A_{\text{wick}}] + \rho_L \times (A_{\text{gap}} + \varepsilon \times A_{\text{wick}}) \tag{8}$$

Figures 10a and 10b show the effects of the aspect ratio on the cross section area and mass of the heat pipe, for $A_V = 314$ mm$^2$, $\delta_{\text{wick}} = 0.2$ mm, $A_{\text{gap}} = 25$ mm$^2$, $\delta_{\text{liner}} = 0.1$ mm, and $L_{\text{ev}} + L_{\text{cd}} = 1.5$ m (the latter is required to calculate the exposed surface area and the thickness of the C–C armor). The thickness of the C–C armor and the exposed and cross-sectional areas of the heat pipe to space are minimum when $\alpha = 0.5$, that is $H_V = R_V$ and $H_W = R_W$ (Figs. 9 and 10a). The perimeter of the wick is also minimum when $\alpha = 0.5$. Because the flow area of the liquid annulus $A_{\text{gap}}$ is kept constant, the liquid annulus thickness changes with $\alpha$, reaching a maximum of 0.359 mm when $\alpha = 0.5$ (Fig. 10b). At this aspect ratio, the wick perimeter and the mass of the armored heat pipe are both minimum (Fig. 10b), which holds true for any given values of $A_V$ and $A_{\text{gap}}$.

**Table 1 Design parameters and materials of the radiator heat pipes**

| Parameter | Value | Parameter | Value |
|---|---|---|---|
| Aspect ratio, $\alpha$ | 0.50 | Wall material/thickness, mm | Ti/0.10 |
| Porous wick material/type | Ti/150-mesh | C–C fin and armor density, kg/m$^3$ | 1800 |
| Wick average porosity | 0.70 | C–C fins thickness, mm | 0.5 |
| Wick effective pore radius, $\mu$m | 50.0 | C–C emissivity | 0.90 |
| Wick thickness, mm/number of layers | 0.20/3 | Space sink temperature, K | 10 |

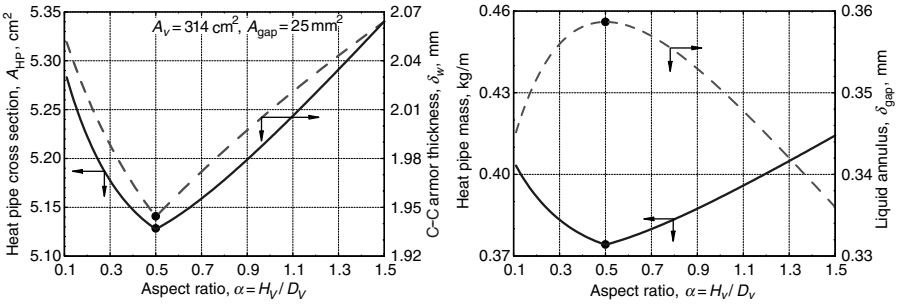


**a) Armor thickness and cross section** **b) Liquid annulus thickness and mass**

**Fig. 10 Effect of aspect ratio $\alpha$ on the heat pipe design and mass.**

Because the mass of the C–C fins is much smaller (<20%) than that of the armored heat pipe, the mass of the radiator segment is minimum when the mass of the heat pipe is minimum, i.e., when $\alpha = 0.5$. Based on these results, an $\alpha$ of 0.5 is used in subsequent radiator analyses. Other design parameters of the rubidium heat pipes are listed in Table 1.

### Heat Pipe Working Fluids

In the SCoRe-TE NRPS, the nominal inlet and exit temperatures of the circulating liquid lithium in the radiator panels (Fig. 6) are 794 and 767 K and the pressure losses in the coolant channels are kept constant at 12 kPa. For these temperatures, a number of alkali-metal working fluids may be considered. This section justifies the selection of rubidium for the heat pipes in the present radiator design. The best performance is typically that corresponding to the maximum FOM of the working fluid $M_L$, defined as (Fig. 11a)

$$M_L = \sigma_L \rho_L h_{fg} / \mu_L \tag{9}$$

FOM has units of W/m$^2$ and changes with temperature. It has a bell shape that covers a certain range of temperatures for each working fluid (Fig. 11a). At low temperatures, the value of the FOM is controlled by the liquid viscosity, which decreases rapidly with increasing temperature. Conversely, at higher temperatures, both the surface tension and the latent heat of vaporization of the working fluid decrease faster than the viscosity with increasing temperature, causing the FOM to decrease (Fig. 11a). The maximum FOM corresponds to the operation temperature at which the effects of decreasing viscosity $\sigma_L$ and $h_{fg}$ are in balance. Unlike water, the curves for the alkali-metal working fluids are quite flat near the maximum FOM, thus enabling a wide range of operation temperatures (Fig. 11a). Ideally, it is better to keep the vapor pressure within the heat pipe $\leq 0.1$ MPa when at nominal operation, and the best performance temperature for a working fluid is that corresponding to the maximum FOM (Fig. 11a). However, operating at this temperature in an NRPS might not be possible due to other practical considerations, such as the type of energy conversion, the low vapor pressure of the heat pipes working fluid (Fig. 11b), and to avoid sonic-limited operation. As shown in Fig. 11a, the FOM of Rb is about 60% higher than that of cesium (Cs), because its surface tension and latent heat of vaporization ($\rho_L h_{fg}$) are higher than those of Cs, whereas the liquid viscosities for Cs and Rb are nearly identical. The FOM of potassium (K) is more than twice that of Rb, because K has higher $\sigma_L$ and $\rho_L h_{fg}$, and lower viscosity.

Other considerations in the selection of the heat pipes working fluid are the values of the capillary and sonic limits. The capillary limit dominates at high temperature when the developed capillary pressure head in the wick, which is proportional to the liquid surface tension, cannot overcome the sum of the vapor and liquid flow pressure losses in the heat pipe. At low vapor Mach number, the pressure losses in the heat pipes are dominated by those of the liquid flow to the evaporator. The sonic limit, which dominates at low temperatures, is inversely proportional to the vapor density, thus the vapor pressure of the selected working fluid is a good indicator of potentially reaching this limit (Fig. 11b). Below ~1 kPa, the vapor flow is not continuum, meaning that the power transport capabilities are limited, and the vapor density is very low, resulting in a high vapor Mach number [16]. The vapor pressures of potassium, rubidium, and cesium are >1 kPa above 700, 640, and 620 K, respectively. Below these temperatures, the sonic limit constrains the operation of the heat pipe, requiring a larger vapor flow area. Based on the values of the vapor pressure, cesium and rubidium are better choices below 800 K, whereas potassium is more appropriate above ~800 K (Fig. 11b) [7]. Other considerations in the selection of the heat pipe working fluid are chemical stability and compatibility with the wall and wick materials, and low melting point. In SCoRe-TE, the radiator heat pipes operate nominally at 700–760 K which are appropriate for using a rubidium working fluid for the heat pipes. The FOM of rubidium is about 60% higher than that of cesium (Fig. 11a), whereas its vapor pressure is nearly identical to that of Cs in the temperature range of interest.

### Performance of Rubidium Heat Pipes

The calculated values of the power throughput and the prevailing operation limits of the rubidium heat pipes in the forward and rear segments of the radiator panel (Fig. 8) are shown in Figs. 12a and 13a as functions of the evaporator wall temperature. The heat pipes in the forward segment have a vapor flow area of 406 mm$^2$ to ensure that the longest heat pipe in the exit-channel (Fig. 8a) nominally operates at 50% of the sonic limit (heat pipe no. 3 in Fig. 12a). This also ensures that all other heat pipes in this segment operate at less than

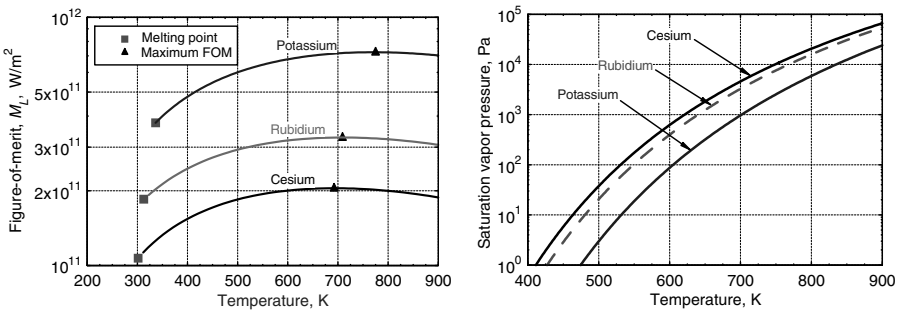


**a) Figure-of-merit** **b) Vapor pressure**

**Fig. 11 Comparison of candidate heat pipe working fluids.**

50% of their sonic limit. The liquid-return annulus in these heat pipes is sized $A_{gap} = 41.3$ mm$^2$, such that the longest heat pipe in the inlet-channel nominally operates at 50% of the capillary limit (heat pipe no. 2 in Fig. 12a). The heat pipes in a radiator segment have an identical cross section, but different C–C armor thickness, which increases with the length of the heat pipe. In the forward segment, the longest heat pipes have a C–C armor that is 1.87-mm-thick, an outer diameter of 2.67 cm, and C–C fin width of 4.20 cm, whereas the C–C armor thickness of the shortest heat pipes is 1.61 mm. These heat pipes have an outer diameter of 2.62 cm and a 4.17-cm-wide C–C fin (see Table 2, column 3).

Figure 12a shows that for the longest heat pipes in the forward radiator segment, the prevailing limit is sonic up to an evaporator wall temperature of 749 K, and is capillary at higher temperatures. Because all heat pipes have the same vapor flow area and a nearly identical radial thermal resistance, they have the same sonic limit. The capillary limit, however, decreases with increasing heat pipe length (Fig. 12a). The shortest heat pipe rejects less heat to space than the longest heat pipe. For example, in the forward segment of the radiator panel (Fig. 8a), the shortest heat pipe of the inlet-channel (no. 1 in Fig. 12a) nominally transports 420 W, whereas the longest heat pipe (no. 2 in Fig. 12a) transports 1.63 kW. The heat pipes attached to the exit coolant channel transport less power than their opposite twins attached to the inlet-channel since the coolant temperature in the former is ~25 K lower (Fig. 12a).

The power throughput and the prevailing operation limits of the heat pipes in the rear segments of the radiator panels (Fig. 8b) are also shown in Fig. 13a. These heat pipes have a vapor flow area of 459 mm$^2$ and a cross section area of the liquid-return annulus $A_{gap} = 29.1$ mm$^2$, to ensure that the longest heat pipes nominally operate at 50% of the prevailing sonic or capillary limit (heat pipes nos. 2 and 3 in Fig. 13a). The longest heat pipes have a C–C armor thickness of 1.84 mm, an outer diameter of 2.77 cm, and C–C fin width of 2.76 cm, whereas the shortest heat pipes have a 1.72-mm-thick C–C armor, a 2.74 cm outer diameter, and 2.75-cm-wide C–C fins (see Table 2, column 4). The C–C fins in the rear segments are shorter than those in the forward segments (Fig. 8a) of the radiator panels, because the former is shorter (5.95 vs 6.61 m) and uses more heat pipes (144 vs 120). Figure 13a also shows that the prevailing limit for the longest heat pipes of the rear segment is sonic up to an evaporator wall temperature of 730 K, and capillary above this temperature.

The temperature drops through the longest heat pipes of the forward and rear segments of the radiator panel are shown in Figs. 12b and 13b, respectively, as functions of evaporator wall temperature. The temperature drops due to conduction in the duct wall, the coolant boundary layer, and the evaporator and condenser structures all increase with increasing evaporator temperature, commensurate with the increase in the power throughput (Figs. 12a and 13a). The temperature drop through the condenser structure is much lower than that through the evaporator structure because the condenser is much longer than the evaporator section. By contrast, the temperature drop in the vapor flow decreases with increasing the evaporator wall temperature because of the increase in the rubidium vapor pressure. The longest heat pipes in the forward and rear

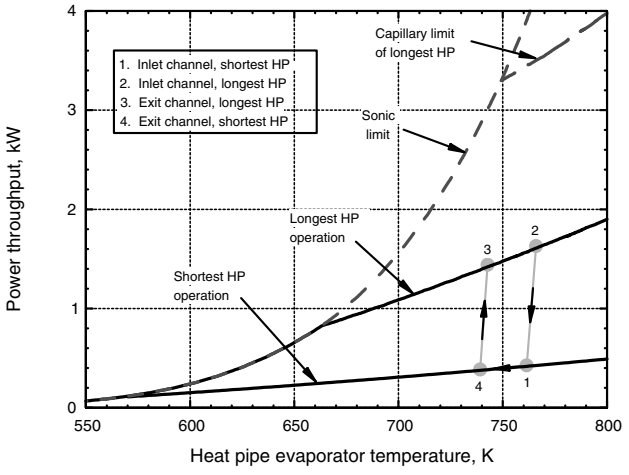


**a) Heat pipe power throughput and limits**

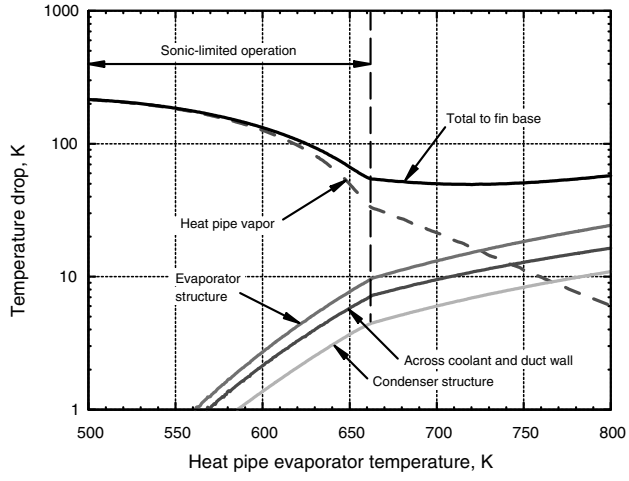


**b) Temperature drops in longest heat pipe**

**Fig. 12 Performance of Rb heat pipes in forward radiator segment.**

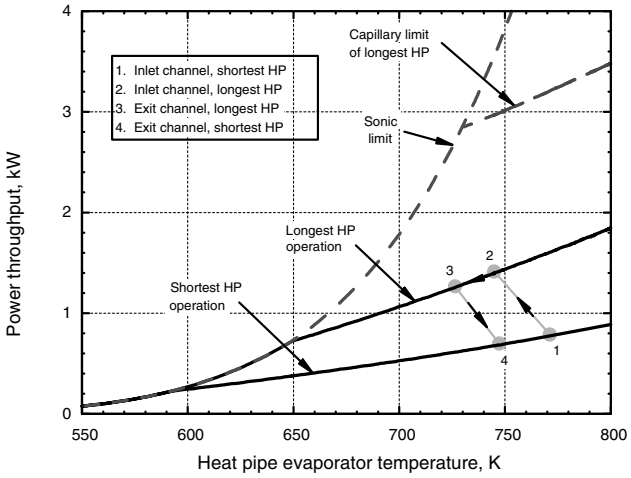


**a) Heat pipe power throughput and limits**

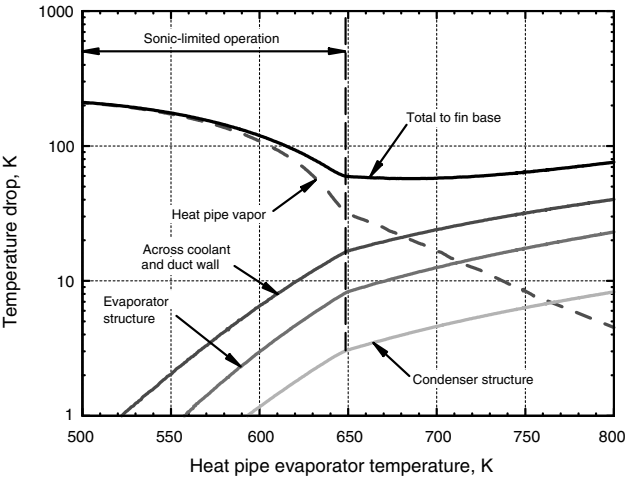


**b) Temperature drops in longest heat pipe**

**Fig. 13 Performance of Rb heat pipes in rear radiator segment.**

**Table 2 Performance comparison of radiators with and without perforated dividers[a]**

| Parameter | Segmented radiator panel without perforated dividers | | Segmented radiator panel with perforated dividers | |
|---|---|---|---|---|
| | *Forward segment* | *Rear segment* | *Forward segment* | *Rear segment* |
| **Geometrical** | | | | |
| Number | 1 | 2 | 1 | 2 |
| Physical surface area, $m^2$ | 9.23 | 9.46 | 9.23 | 9.46 |
| Effective radiation view factor | 1.06 | 1.273 | 1.06 | 1.273 |
| Length, m | 6.605 | 5.952 | 6.605 | 5.952 |
| Height of flow channel, cm | 1.52 | 1.545 | 0.822 | 1.177 |
| Orifice diameter, mm | NA | NA | 1.0 | 1.0 |
| Orifices number density #/$cm^2$ | NA | NA | 1.9–3.5 | 0.75–8.5 |
| Shortest heat pipe length, cm | 26.8 | 59.0 | 26.8 | 59.0 |
| Longest heat pipe length, cm | 113.0 | 100.0 | 113.0 | 100.0 |
| Shortest heat pipe evaporator, cm | 4.0 | 8.0 | 4.0 | 8.0 |
| Longest heat pipe evaporator, cm | 10.0 | 8.0 | 10.0 | 8.0 |
| Number of heat pipes | 120 | 144 | 120 | 144 |
| Heat pipe outer diameter, cm | 2.62–2.67 | 2.74–2.766 | 2.62–2.67 | 2.74–2.766 |
| C–C fin width, cm | 4.17–4.2 | 2.75–2.76 | 4.17–4.2 | 2.75–2.76 |
| Vapor flow area in heat pipe, $mm^2$ | 406 | 459 | 406 | 459 |
| Liquid annulus in heat pipe, $mm^2$ | 41.3 | 29.1 | 41.3 | 29.1 |
| Annular gap in heat pipe, mm | 0.520 | 0.348 | 0.520 | 0.348 |
| C–C armor thickness, mm | 1.612–1.867 | 1.718–1.844 | 1.612–1.867 | 1.718–1.844 |
| Lithium coolant volume, liters | 14.0 | 14.65 | 7.56 | 11.16 |
| **Performance parameters** | | | | |
| Lithium flow rate, kg/s | 1.09 | 1.50 | 1.111 | 1.485 |
| Heat rejection load, $kW_{th}$ | 114.2 | 157.2 | 116.4 | 155.6 |
| Mass of heat pipes, kg | 34.87 | 47.65 | 34.87 | 47.65 |
| Mass of C–C fins, kg | 6.32 | 5.69 | 6.32 | 5.69 |
| Mass of coolant channels wall, kg | 3.83 | 3.87 | 3.58 | 3.76 |
| Mass of channels armor, kg | 2.31 | 2.38 | 2.31 | 2.38 |
| Mass of support structure, kg | 3.02 | 3.80 | 3.00 | 3.80 |
| Total dry mass, kg | 50.35 | 63.39 | 50.08 | 63.28 |
| Dry specific mass, $kg/m^2$ | 5.46 | 6.70 | 5.43 | 6.69 |
| Total wet mass, kg | 57.58 | 70.97 | 54.00 | 69.05 |
| Wet specific power, $kW_{th}/kg$ | 1.98 | 2.21 | 2.16 | 2.25 |
| Panel mass flow rate, kg/s | 4.09 | | 4.081 | |
| Panel heat rejection, $kW_{th}$ | 428.5 | | 427.6 | |
| Panel dry mass, kg | 177.13 | | 176.64 | |
| Lithium mass in panel, kg | 22.39 | | 15.46 | |
| Lithium volume in panel, liters | 43.3 | | 29.88 | |
| Panel total mass, kg | 199.5 | | 192.1 | |
| Panel specific mass, $kg/m^2$ | 7.09 | | 6.82 | |
| Panel specific power, $kW_{th}/kg$ | 2.15 | | 2.23 | |

[a]Calculations are for a pressure drop of 12 kPa and lithium coolant inlet and exit temperatures of 780 and 755 K, respectively.

segments of the radiator panel, with vapor flow areas of 406 and 459 $mm^2$, are sonic-limited at evaporator wall temperatures of 662 and 648 K (Figs. 12b and 13b). The total temperature drop between the lithium coolant flow in the channels of the radiator segment and the base of the C–C fin is lowest when the heat pipe is not sonic-limited, and increases slowly with increasing temperature as the power throughput increases. When operating at an evaporator wall temperature of 750 K, the longest heat pipes in the forward and rear segments of the radiator panels each transports 1.48 and 1.44 kW. The temperature drop between the Li coolant and channel wall is 12.8 and 31.7 K, in the evaporator structure is 18.4 and 17.6 K, in the vapor is 11.2 and 8.4 K, and is 8.3 and 6.3 K in the condenser structure. The total temperature drop between the lithium coolant and the base of the C–C fins is 50.7 and 64 K, respectively (Figs. 12b and 13b).

The temperature drop between the Li coolant and the channel wall at the longest heat pipe in the rear segments is 31.7 vs 12.8 K in the forward segments. This is because the Li convective heat transfer coefficient in the rear segment is much smaller, and the heat pipe evaporator length (and consequently the heat transfer area) is smaller (8 vs 10 cm in the forward segments). In the forward radiator segments, the lithium coolant enters at the end where the longest heat pipes are laid out and the Li mass flow rate is highest, with an axial Reynolds number of 80,000 and a convective Nusselt number of 15. By contrast, in the rear segments, the longest heat pipes are located at the back end of the inlet and exit coolant channels, where the lithium flow rate is lowest, with an axial Reynolds number of only 5,000 and corresponding Nusselt number of only 6.5.

**Performance of Radiator Panel Segments**

The nominal performance results of the forward and rear radiator segments for lithium coolant entering the radiator panel at 780 K and exiting at 755 K ($\Delta T = 25$ K) are shown in Figs. 14 and 15. In these figures, $z/L = 0$, 1, and 2 correspond to the entrance, the back end, and the exit of the coolant channel in a radiator panel segment, respectively. As mentioned earlier, the longest heat pipes in the forward radiator segment are at $z/L = 0$ and $z/L = 2$, but at $z/L = 1$ in the rear segment (Figs. 7 and 8). The orifices in the divider between the inlet and exit coolant channels in the forward and rear segments are optimized to ensure nearly uniform, but different temperatures in these channels. The heat pipes attached to the inlet-channel and their C–C fins operate at higher temperature and reject more thermal power than those attached to the exit-channel (Figs. 14 and 15).

The power throughput of the heat pipes varies almost linearly with axial distance along the radiator segments (Figs. 14a and 15a), commensurate with the effective surface area. The longest heat pipes on the inlet- and exit-channels of the forward segments of the radiator are 1.13-m-long and transport 1.68 and 1.49 kW, whereas the shortest heat pipes (26.8-cm-long) transport only 377 and 335 W. The longest heat pipes at the inlet and the exit of the coolant channels in the rear segments are 100-cm-long and transport 1.43 and 1.29 kW, respectively, whereas the shortest heat pipes (59-cm-long) transport 758 and 670 W, respectively (Fig. 15a). The forward radiator segment with 120 heat pipes and an effective surface area of 9.78 $m^2$ nominally rejects 116.4 kW, whereas each rear radiator segment with 144 heat pipes and a higher effective area of 12.04 $m^2$ nominally rejects 155.6 kW. Each radiator panel, with one forward

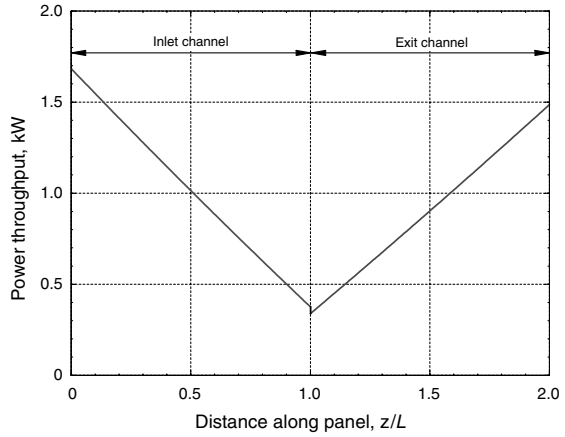


a) Power throughput

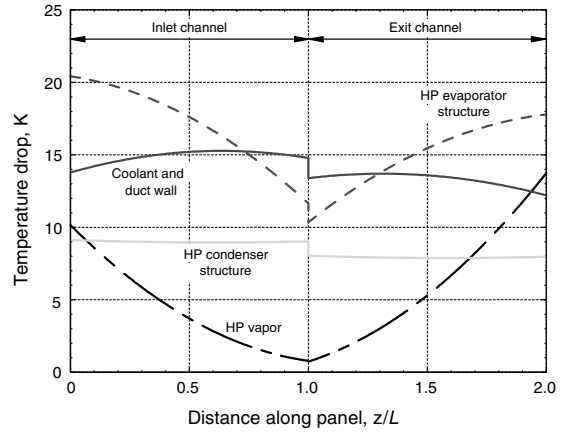


b) Temperature drops

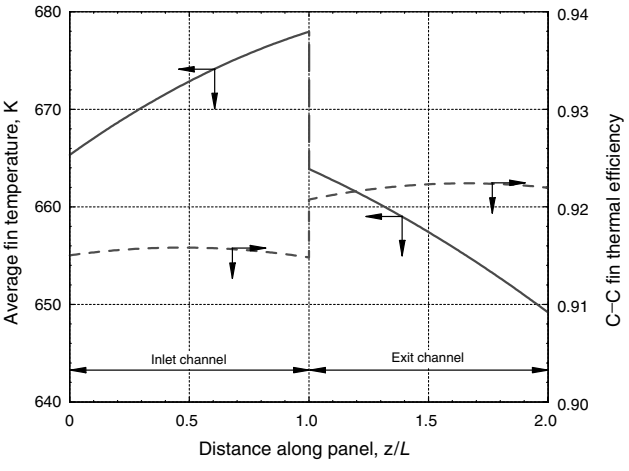


c) C–C fin temperature and efficiency

**Fig. 14 Thermal performance of forward radiator segment.**

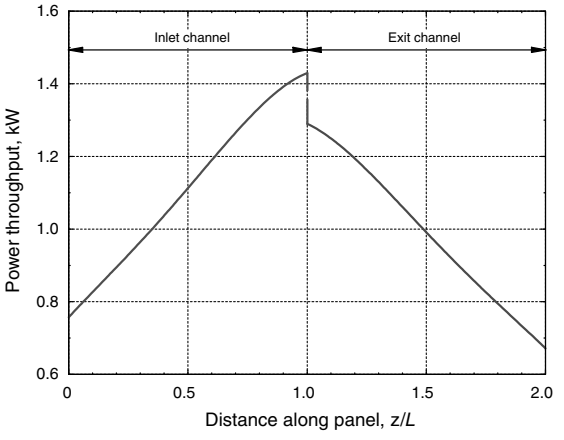


a) Power throughput

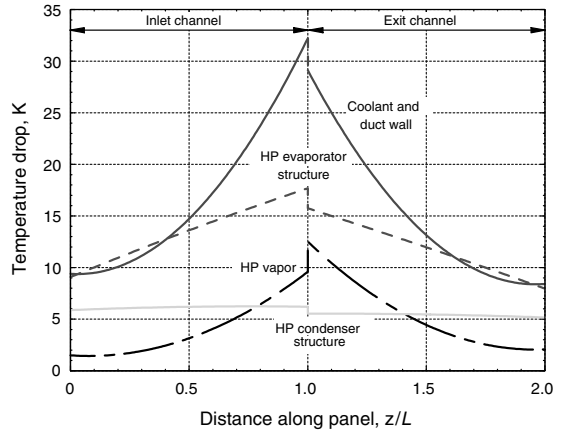


b) Temperature drops

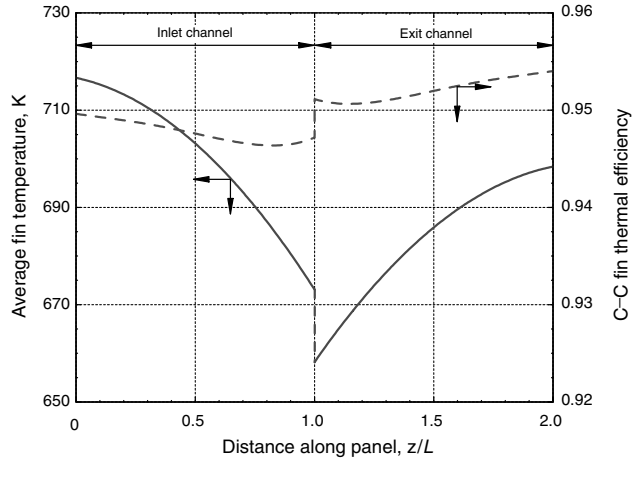


c) C–C fin temperature and efficiency

**Fig. 15 Thermal performance of rear radiator segment.**

segment and two rear segments, rejects nominally 427.6 kW, and has a specific power of 2.23 kW/kg (Table 2).

The calculated axial distributions of the temperature drops along the forward and rear segments are shown in Figs. 14b and 15b, respectively. Typically, the longer the heat pipes the larger are the temperature drops, because longer heat pipes transport more thermal power. The temperature drop through the condenser structure of the heat pipes, however, is nearly constant because the heat transported by the heat pipe is proportional to the condenser length (Figs. 14b and 15b). The changes in the temperature drop in the lithium coolant and the channel walls, however, are different for the forward and rear segments of the radiator panel. In the forward segment, this temperature drop is nearly constant, but different, along each channel (Fig. 14b). This is because the axial mass flow rate in the coolant channel, the convective heat transfer coefficient, and the evaporator length of the heat pipes all increase with increasing heat pipe length. In the rear radiator segments, the temperature drop through the lithium coolant and the channel wall is much larger under the longest heat pipes (∼30 K) than under the shortest heat pipes (∼10 K) (Fig. 15b).

Generally, the C–C fins of the long heat pipes are cooler than those of the short heat pipes, because the former transports more power and experiences a larger overall temperature drop (Figs. 14c and 15c). In addition, the C–C fins of the heat pipes of a radiator segment on the inlet-channel are hotter than of the heat pipes on the exit-channel. Because the thermal conductivity of C–C decreases rapidly with

increasing temperature, the efficiencies of the fins on the exit-channel are higher than of the fins on the inlet-channel (Figs. 14c and 15c). The C–C fins in the forward radiator segment have a thermal efficiency of ~92%, whereas those in the rear segment have a higher efficiency of ~95%. This is because the C–C fins are wider (4.2 cm) in the forward segment than in the rear segments (2.8 cm). The rear radiator segment is shorter (5.95 m) and has more heat pipes (144) than the forward segment (6.61-m-long) which employs less (120) heat pipes (Table 2, columns 3 and 4).

## Thermal-Hydraulics of Coolant Channels of Radiator Panel

In this section, a detailed thermal-hydraulics model of the forward and rear segments of the radiator panel segment is developed to reduce the cross section area of the coolant channels, and hence the lithium liquid inventory and the radiator mass. To reduce the lithium liquid inventory in the radiator panel 1) the three segments (one forward and two rear) of each panel are hydraulically connected in parallel, while the total pressure loss is constant at 12 kPa (Fig. 6); and 2) perforated dividers are used between the lithium inlet- and exit-channels. The orifices in these dividers are 1.0 mm in diameter, but their number density changes along the coolant channels.

### Thermal-Hydraulic Model

This model discretizes the inlet and exit coolant channels in the radiator segment into $N$ small axial sections (Fig. 16), each providing thermal energy by convection from the flowing lithium to a few (five or six) rubidium heat pipes with C–C fins. In each section, the model solves the coupled momentum and energy balance equations for the lithium flow and calculates the change in lithium temperature in the inlet- and exit-channels. It also calculates the temperature drops through the channel walls and the heat pipes evaporator structure. The present radiator performance analysis is for fixed lithium inlet and exit temperatures of 780 and 755 K, respectively. As a result, the Li mass flow rate in each radiator segment is proportional to the heat rejection capability of the segment.

The thermal-hydraulic model is coupled to a heat pipe model, which calculates the vapor pressure losses and the temperature drop along the heat pipes and through the evaporator and the condenser structures to the base of the C–C fins. It also calculates the heat pipes sonic, capillary, entrainment, and incipient boiling limits, to ensure a sufficient nominal operation design margin. The coupled radiator-heat pipe model calculates the local radiation view factor of the radiator and the effective fin efficiency for rejecting waste heat into space.

The rate of heat rejection from each half-segment $\{i\}$ (one each on the inlet- and exit-channels) of the radiator panel is the sum of those from the condenser walls of the $n_{\rm HP}/(2N)$ heat pipes $Q_i^{\rm HP}$ and from the attached C–C fins $Q_i^{\rm fin}$, which are given, respectively, by

$$Q_i^{\rm HP} = \sigma\varepsilon F_i[n_{\rm HP}/(2N)] \times (2R_w L_{\rm cd})_i \times [(T_i^{\rm cd})^4 - T_{\rm sink}^4] \qquad (10)$$

where $T^{\rm cd}$ is the average surface temperature of the condenser wall of the heat pipes, and

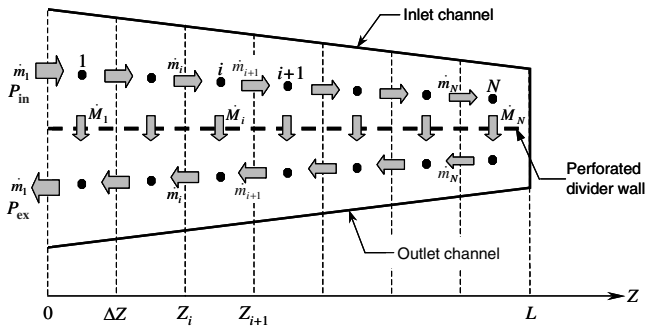


**Fig. 16 Lithium coolant distribution in channels and across perforated divider for numerical calculations.**

$$Q_i^{\rm fin} = \sigma\varepsilon F_i[n_{\rm HP}/(2N)] \times (2W_{\rm fin}L_{\rm cd})_i \times \eta_i^{\rm fin} \times [(T_i^{\rm base})^4 - T_{\rm sink}^4] \qquad (11)$$

The local thermal efficiency of the C–C fin is given as [17]

$$\eta_i^{\rm fin} = \tanh(h^*)/h^* \quad \text{with} \quad h^* = \sqrt{\bar h_i^{\rm fin} \times W_{\rm fin}^2/(\delta_{\rm fin}\bar k_i^{\rm fin})} \qquad (12)$$

The fin average radiative heat transfer coefficient is given by

$$\bar h_i^{\rm fin} = \sigma\varepsilon F_i \times [(\bar T_i^{\rm fin})^2 + T_{\rm sink}^2] \times (\bar T_i^{\rm fin} + T_{\rm sink}) \qquad (13)$$

The average fin temperature $\bar T_i^{\rm fin}$ is a function of the space sink temperature and the fin base temperature as

$$\bar T_i^{\rm fin} = T_{\rm sink} + \eta_i^{\rm fin} \times (T_i^{\rm base} - T_{\rm sink}) \qquad (14)$$

The model of the radiator panel segment calculates the pressure drops along the lithium flow channels and across the orifices in the perforated dividers between the inlet- and exit-channels, and the change in the coolant flow rate along the channels (Fig. 16). The number density of the orifices in the dividers is optimized to ensure proper bleeding rates between the inlet- and exit-channels. The axial mass flow rate in the coolant channel, between sections $\{i-1\}$ and $\{i\}$, $\dot m_i$, and the crossflow through the orifices in section $\{i\}$, $\dot M_i$, are related by the conservation of mass in the channels (Fig. 16) as

$$\dot m_{\rm in} = \dot m_1 = \sum_{j=1}^{N} \dot M_j \qquad (15a)$$

and

$$\dot m_i = \dot m_1 - \sum_{j=1}^{i-1} \dot M_j \qquad (15b)$$

The crossflow rate through the orifices in each axial section is proportional to the heat rejection from that section:

$$\dot M_i = Q_i/(C_p\Delta T) = \dot m_1 \times Q_i \Big/ \sum_{j=1}^{N} Q_j \qquad (16)$$

The heat rejection capability of each axial section $Q_i = (Q_i^{\rm HP} + Q_i^{\rm fin})^H + (Q_i^{\rm HP} + Q_i^{\rm fin})^C$ is calculated by the radiator model. The axial pressure losses in the inlet and exit coolant channels are calculated, respectively, as

$$\Delta P_i^H = f_i^H\left(\frac{L_i}{D_i}\right)\frac{\dot m_i^2}{2\rho_{\rm in}A_i^2} = \frac{a}{2}\frac{\mu_{\rm in}^b}{\rho_{\rm in}}\left(\frac{L_i}{D_i^{1+b}A_i^{2-b}}\right)\dot m_i^{2-b} = C_i^H \times \dot m_i^{2-b} \qquad (17a)$$

and

$$\Delta P_i^C = f_i^C\left(\frac{L_i}{D_i}\right)\frac{\dot m_i^2}{2\rho_{\rm ex}A_i^2} = \frac{a}{2}\frac{\mu_{\rm ex}^b}{\rho_{\rm ex}}\left(\frac{L_i}{D_i^{1+b}A_i^{2-b}}\right)\dot m_i^{2-b} = C_i^C \times \dot m_i^{2-b} \qquad (17b)$$

The geometrical parameters in Eqs. (17a) and (17b) are defined as

$$L_1 = L/(2N) = 0.5\Delta Z, \qquad L_i = L/N = \Delta Z \quad \text{for } i = 2 \text{ to } N$$
$$A_i = H \times W_i, \quad \text{and} \quad D_i = 2 \times H \times W_i/(H + W_i) \qquad (18)$$

The values of the coefficients $a$ and $b$ for the friction factor $f = a/Re^b$ depend on the local Reynolds number. For the Blasius turbulent flow regime of interest $5000 < Re < 300,000$, $a = 0.316$ and $b = 0.25$.

The number density of the orifices in the divider between the inlet- and exit-channels in section $\{i\}$ satisfies the momentum balance along each flow path $\{i\}$, starting at the entrance of the inlet-channel and flowing through the orifices in the divider in section $\{i\}$ to the exit of the return coolant channel, thus

$$\Delta P_{\rm rad} = \sum_{j=1}^{i} \Delta P_j^H + \Delta P_i^{\rm orif} + \sum_{j=1}^{i} \Delta P_j^C \quad \text{for } i = 1 \text{ to } N \qquad (19)$$

The pressure drop through the sharp-edged orifices of the divider

between the inlet and exit flow channels is given as [18]

$$\Delta P_i^{\text{orif}} = \frac{K_i^{\text{orif}}}{2\bar{\rho}}\left(\frac{\dot{M}_i}{A_i^{\text{orif}}}\right)^2 = \frac{K_i^{\text{orif}}}{\beta_i^2}\times\frac{1}{2\bar{\rho}}\left(\frac{\dot{M}_i}{H\Delta Z}\right)^2 = C_i^{\text{orif}}\times\dot{M}_i^2 \quad (20)$$

The dimensionless loss coefficient of the orifices is given as [18]

$$K_i^{\text{orif}} = K_i^{\text{dis}} + \varepsilon_i^o \times K_i^{\text{turb}} \quad (21)$$

where

$$K_i^{\text{dis}} = \frac{10}{(Re_i^{\text{orif}} - 20)^{0.45}} - \frac{45}{Re_i^{\text{orif}} - 2} \quad (22a)$$

$$\varepsilon_i^o = 1 + \frac{2006}{Re_i^{\text{orif}} + 692} - \frac{229}{(Re_i^{\text{orif}} + 470)^{0.676}} \quad (22b)$$

$$K_i^{\text{turb}} = (1 - \beta_i + 0.707\sqrt{1-\beta_i})^2 \quad (22c)$$

These coefficients are plotted in Fig. 17 as functions of $\beta$ and the Reynolds number through the orifices

$$Re_i^{\text{orif}} = \frac{\dot{M}_i d_{\text{orif}}}{\bar{\mu}A_i^{\text{orif}}} = \frac{\dot{M}_i d_{\text{orif}}}{\bar{\mu}\beta_i(H\Delta Z)} \quad (23)$$

The orifices number density (number of orifices per unit area of divider) is given as

$$N_i'' = 4\beta_i/(\pi\, d_{\text{orif}}^2) \quad (24)$$

As shown in Fig. 17b, the discharge loss coefficient is relatively large (2 at $Re^{\text{orif}} = 30$) at low orifices Reynolds number, but decreases precipitously with increasing $Re^{\text{orif}}$, approaching zero in the turbulent flow regime. This coefficient is essentially independent of the orifices area ratio $\beta$ (Fig. 17b). On the other hand, the orifices pressure loss correction factor $\varepsilon^o$ increases with increasing $Re^{\text{orif}}$, approaching an asymptote of unity at large $Re^{\text{orif}} > 10^5$ (Fig. 17a). As a result, the orifices loss coefficient given by Eq. (21) is reduced to the turbulent loss coefficient $K^{\text{turb}}$ at $Re^{\text{orif}} > 10^5$ (Fig. 17c). Note that $K^{\text{turb}}$, given by Eq. (22c), is independent of the orifices diameter and Reynolds number and only a function of the orifices area ratio $\beta_i$. The radiator segment model iteratively calculates the orifices area ratio $\beta_i$, such that the pressure drop $\Delta P_i^{\text{orif}}$ predicted by Eq. (20) matches that calculated from the momentum balance Eq. (19) along the lithium flow path $\{i\}$ to where the orifices are located. Substituting Eq. (19) into Eq. (20) gives the following expression of the orifices coefficient $C_i^{\text{orif}}$:

$$C_i^{\text{orif}} = \Delta P_i^{\text{orif}}/\dot{M}_i^2 = \left(\Delta P_{\text{rad}} - \sum_{j=1}^{i}\Delta P_j^H - \sum_{j=1}^{i}\Delta P_j^C\right)/\dot{M}_i^2 \quad \text{for } i = 1 \text{ to } N \quad (25)$$

This coefficient is a complex function of $\beta_i$ (see Eqs. (20–23)), thus Eq. (25) is solved iteratively for $\beta_i$ using the SIMULINK algebraic loop solver [19,20].

Once the orifices area ratio along the divider $\beta_i$ is determined, the flow, pressure, and temperature distributions in the radiator segment are calculated from solving the continuity, momentum, and energy balance equations. Subtracting Eq. (19) for $\{k = i-1\}$ from the momentum balance Eq. (19) for $\{k = i\}$ gives

$$\Delta P_i^H + \Delta P_i^C + \Delta P_i^{\text{orif}} - \Delta P_{i-1}^{\text{orif}} = 0 \quad \text{for } i = 2 \text{ to } N \quad (26a)$$

or

$$(C_i^H + C_i^C)\times\left(\dot{m}_{\text{in}} - \sum_{k=1}^{i-1}\dot{M}_k\right)^{2-b} + C_i^{\text{orif}}\times\dot{M}_i^2 - C_{i-1}^{\text{orif}}\times\dot{M}_{i-1}^2 = 0 \quad \text{for } i = 2 \text{ to } N \quad (26b)$$

where the axial mass flow rate $\dot{m}_i$ is substituted for in terms of the crossflow rates using the continuity Eq. (15b). Equations (26b), for $i = 2$ to $N$, and the overall mass balance Eq. (15a),

$$\sum_{k=1}^{N}\dot{M}_k = \dot{m}_{\text{in}}$$

are solved simultaneously for the crossflow rates $\{\dot{M}_j\}$, $j = 1$ to $N$, using the SIMULINK algebraic loop solver [19,20]. This solver uses

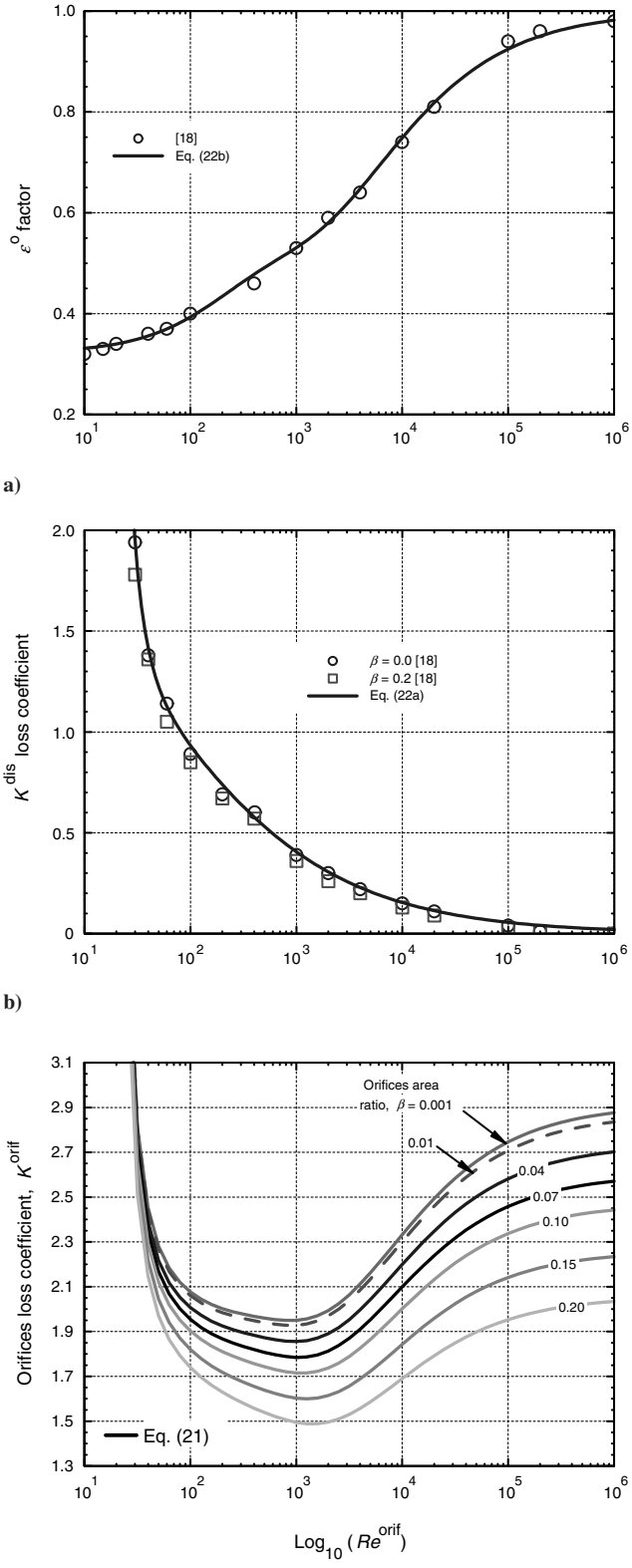


**Fig. 17 Coefficients for calculating pressure loss through orifices in perforated dividers.**

a Newton method with weak line search and a Jacobian matrix of partial derivatives, because the Eqs. (26b) are not linear in the crossflow rates. Once the crossflow rates $\dot{M}_i$ are obtained, the axial mass flow rates $\dot{m}_i$ are calculated using the continuity Eq. (15b), and the total coolant pressure drop through the radiator panel is obtained from the momentum balance Eq. (19) for $\{i = 1\}$, as

$$\Delta P_{\text{rad}} = \Delta P_1^H + \Delta P_1^C + \Delta P_1^{\text{orif}} = (C_1^H + C_1^C) \times \dot{m}_{\text{in}}^{2-b} + C_1^{\text{orif}} \times \dot{M}_1^2 \tag{27}$$

The lithium properties are temperature dependent, and the lithium coolant temperature is obtained from the simultaneous solution of the steady-state energy balance equations (Fig. 16):

$$\dot{m}_i \times (C_p T_b)_i^{H,\text{in}} - \dot{m}_{i+1} \times (C_p T_b)_i^{H,\text{ex}} - \dot{M}_i \times (C_p T_b)_i^{\text{orif}} = (Q_i^{\text{HP}} + Q_i^{\text{fin}})^H - \Phi_{H,i}^{\text{vis}} \tag{28a}$$

and

$$\dot{m}_{i+1} \times (C_p T_b)_i^{C,\text{in}} - \dot{m}_i \times (C_p T_b)_i^{C,\text{ex}} + \dot{M}_i \times (C_p T_b)_i^{\text{orif}} = (Q_i^{\text{HP}} + Q_i^{\text{fin}})^C - \Phi_{C,i}^{\text{vis}} \tag{28b}$$

for section $\{i\}$ of the inlet and exit coolant channels, respectively. The heat rejection to space from the surfaces of the heat pipes and the attached C–C fins, $Q_i^{\text{HP}}$ and $Q_i^{\text{fin}}$, are given by Eqs. (10) and (11) as functions of temperatures.

**Coolant Channel Cross-Sectional Areas**

The effects of thermal-hydraulically coupling the three segments of each panel in parallel, and of using perforated dividers, on the cross section flow areas and hence, the lithium coolant inventory, are investigated by changing the height of the inlet- and exit-channels (Fig. 18). The results in this figure are for the forward radiator segment with an inlet mass flow rate of 1.111 kg/s, a total pressure drop of 12 kPa, inlet and exit coolant temperatures of 780 and 755 K, a fixed orifices diameter of 1 mm, and three different values of the channels height $H$. The axial flow rate decreases with distance along the coolant channels because of the crossflow through the orifices in the divider between the inlet- and exit-channels (Fig. 18a). For a relatively large $H = 1.6$ cm, the coolant pressure in the inlet-channel decreases very little, slightly below the inlet pressure of 30 kPa. Similarly, the pressure in the exit-channel is slightly above that at the radiator exit of 18 kPa (Fig. 18b). Because axial pressure losses are small, the orifices pressure drop (the difference between the inlet- and exit-channels pressures) decreases only slightly with axial distance along the coolant channels (Fig. 18d). For this channels height, the orifices number density is $<1$ cm$^{-2}$ and decreases with distance along the channels due to the decrease in crossflow rate (Fig. 18c), which is proportional to the slope of the axial flow rate shown in Fig. 18a.

For the forward radiator segment, decreasing the channels height increases the axial pressure losses and decreases the orifices pressure drop, increasing their number density, because the local crossflow rate along the coolant channels is unchanged. For $H = 0.92$ cm, the orifices pressure drop decreases from 12 kPa at the entrance to only 3.5 kPa at the back end of the inlet-channel (Fig. 18d). The pressure distribution in the channels of the forward radiator segment with $H = 0.822$ cm is also shown in Figs. 18b and 18d. With this channels height, the axial pressure losses in the inlet- and exit-channels are nearly equal to their maximum value of $12/2 = 6$ kPa, and the orifices pressure drop decreases sharply to nearly zero at the back end of the channels (Fig. 18d). This sharp decrease causes the orifices number density to increase with distance along the channel until it reaches a peak, then decreases with further increase in distance along the channel (Fig. 18c), where the orifices pressure drop is very small and nearly constant. Such a decrease in $N''_{\text{orif}}$ with axial distance is proportional to the decrease in crossflow rate through the orifices (Fig. 18c). Since the lithium coolant inventory in the channels increases with increasing the channel height $H$, it is preferable to use the smallest height.

Figures 19a and 19b show the results on the effect of changing $H$ on the orifices fractional pressure losses and area ratio at the back end of the channels of the forward radiator segment. Note that the orifices number density and area ratio are related by $N''_i = 4\beta_i/(\pi\, d_{\text{orif}}^2)$. Figure 19b shows the lithium coolant volume in the channels of the forward radiator segment, which is proportional to the height of the channels. In the limiting cases when the orifices-to-radiator pressure ratio is zero (Fig. 19a), $\beta_N$ is unity (Fig. 19b), which corresponds to the smallest possible values of $H$ for a given total pressure drop. These values are 0.941, 0.817, and 0.740 cm

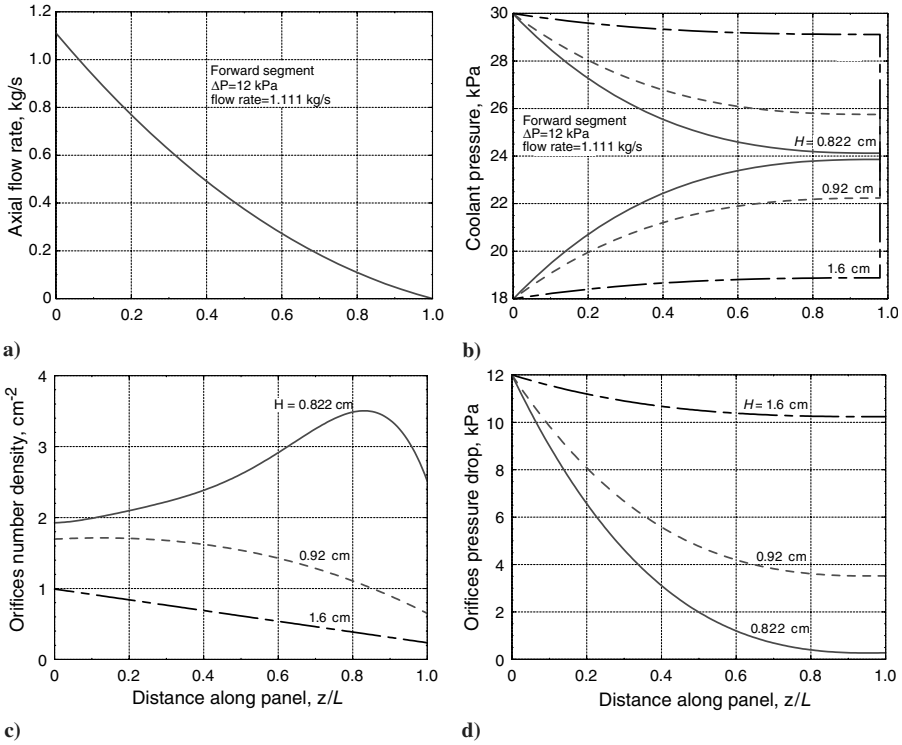


**Fig. 18 Effects of $H$ on pressure losses and $N''_{\text{orif}}$ in forward coolant channel.**

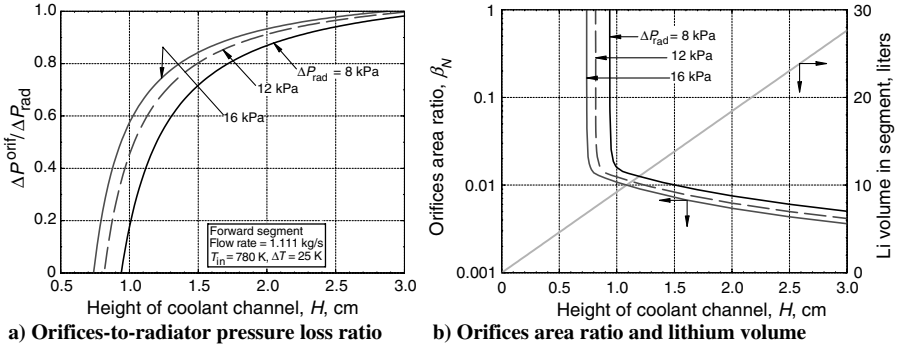


**a) Orifices-to-radiator pressure loss ratio** **b) Orifices area ratio and lithium volume**

**Fig. 19 Effects of $H$ and $\Delta P_{rad}$ on design of forward segment channel.**

when the total pressure losses are 8, 12, and 16 kPa, respectively, (Fig. 19a), which corresponds to lithium coolant inventories of 8.68, 7.53, and 6.82 liters, respectively. Note that the effect of the total pressure losses in the radiator panel on the lithium inventory in the secondary loop of the SCoRe-TE NRPS is relatively small, because the inventory in the forward and rear segments of the radiator (Fig. 7) represents <50% of the total lithium inventory in the secondary loop. For example, decreasing the radiator pressure losses from 16 to 12 kPa increases the lithium inventory in the forward and rear segments of the radiator by only 10% and in the secondary loop by 5%.

In this work, the height of the coolant channels in the radiator segments is chosen such that $\beta_N$ does not exceed 10%. For the forward segment of the radiator when $\Delta P_{rad} = 12$ kPa, $H = 0.822$ cm, which is only 0.6% higher than the lowest value of 0.817 cm (Fig. 19a).

#### Thermal-Hydraulic Performance

Based on the above analysis, the lithium coolant channels in the forward segments of the radiator panel for the SCoRe-TE NRPS are 0.822 cm high and their width is tapered linearly between 10 cm at the inlet to 4 cm at the back end of the channel (Fig. 8a). By contrast, the coolant channels of the rear segments of the radiator panel are rectangular with a constant width of 8 cm and height of 1.177 cm (Table 2 and Fig. 8b). Figures 20a–20f show the thermal-hydraulic performance of the lithium coolant in the forward and rear segments of the radiator panel at nominal operation. The rear segments operate at a higher lithium mass flow rate (1.485 kg/s) than the forward segments (1.111 kg/s, Fig. 20a), because the former have higher effective surface area (12.04 $m^2$) and heat rejection rate (155.6 kW) than the latter (9.78 $m^2$ and 116.4 kW, respectively, see Table 2). The slope of the axial lithium mass flow rates in the radiator channels in Fig. 20a is controlled by the heat rejection rate and the crossflow rate through the perforated divider between the channels. The crossflow rate is highest at the location of the longest heat pipes, $z/L = 0$ and $z/L = 2$ in the forward segment, and $z/L = 1$ in the rear segment (Fig. 20b), and is lowest at the location of the shortest heat pipes. As shown in Fig. 20c, the lithium temperature in the inlet-channels is nearly uniform and slightly lower than the inlet temperature of 780 K, while that in the exit-channels is slightly lower than the exit temperature of 755 K. The fact that the coolant temperature distribution is not exactly a step function is due to the fact that the heat rejection is not distributed evenly across the channels. The heat pipes and C–C fins attached to the inlet-channels operate at higher temperature and therefore reject more thermal power than those attached to the exit-channels (Figs. 14 and 15).

The changes in the orifices number density and Reynolds number along the coolant channels, for a total pressure drop of 12 kPa, are shown in Fig. 20d. For the forward radiator segments, the rapid decrease in the orifices pressure drop (Fig. 20e) increases their number density along the channel (Fig. 20d) until it peaks, then decreases with further increase in axial distance along the coolant channel, where the orifices pressure drop is low and the crossflow rate continues to decrease (Fig. 20b). By contrast, the orifices number density in the channels divider of the rear radiator segments always increases with distance along the channels, due to the combined effects of both the increase in the crossflow rate (Fig. 20b) and the decrease in the orifices pressure drop (Fig. 20f). The changes in the lithium coolant pressure along the channels of the forward and rear radiator segments are nearly identical (Figs. 20e and 20f). For the selected coolant channels heights of $H = 0.822$ and 1.177 cm in the forward and rear segments, respectively, the orifices pressure drop at the back end of the channels in the forward and rear segments are only 260 and 400 Pa, respectively, or 2.2 and 3.3% of the total pressure drop of 12 kPa.

## Effects of Tapering Coolant Channels

In this section, the effect of tapering the width of the coolant channels on the radiator's performance is investigated. For the forward radiator segment, the average width of each channel is kept constant at 7 cm, whereas in the rear segment, the average width of the channels is 8 cm. The effect of changing the coolant channels width ratio, $W_{back}/W_{in}$ on the performance of the forward and rear segments of the radiator is investigated. The channel width is tapered and varied linearly between $W_{in}$ and $W_{back}$. A width ratio of 1.0 means that the coolant channel cross section is constant and equal to the mean value, and a width ratio of 0.5 means that the width of the inlet-channel is twice that at the back end. Results for the forward and rear segments of the radiator are shown in Figs. 21 and 22, respectively.

#### Forward Radiator Segments

In the forward radiator segments, the longest heat pipes are located at the entrance of the coolant channel, thus only width ratios <1 are of interest, that is, the channel width (or heat pipe evaporator length) is larger at the entrance than at the back end of the coolant channels. Because the longest heat pipes transport more thermal power, the highest vapor Mach number occurs in the longest heat pipe at the exit of the coolant channel, which runs the coolest. Decreasing the width ratio of the coolant channels in the forward segments of the radiator shortens the evaporator length of the longest heat pipes, increasing the thermal resistance and decreasing the vapor pressure (Fig. 20b). As a result, the vapor flow area must increase to ensure that the vapor Mach number at the evaporator exit is $\leq 0.50$ (Fig. 21a).

By contrast, capillary is the constraining limit in the longest heat pipe of the inlet-channel because it operates at higher temperature and transports more thermal power than the longest heat pipe of the exit-channel. The operating temperature of the longest heat pipes decreases with increasing $W_{back}/W_{in}$ (Fig. 21b) due to the decrease in the evaporator length. Conversely, the temperature of the average heat pipes, located midway between the inlet and back end of the coolant channels, increases slowly with $W_{back}/W_{in}$. For these heat pipes, the evaporator length remains unchanged and equal to the average width of the channels (7 cm), but their thermal resistance decreases because $A_V$ increases and the thickness of the liquid annulus decreases (Fig. 21a). The temperature of the shortest heat pipes in the forward radiator segments increases much quicker with increasing $W_{back}/W_{in}$, since the evaporator length of these heat pipes

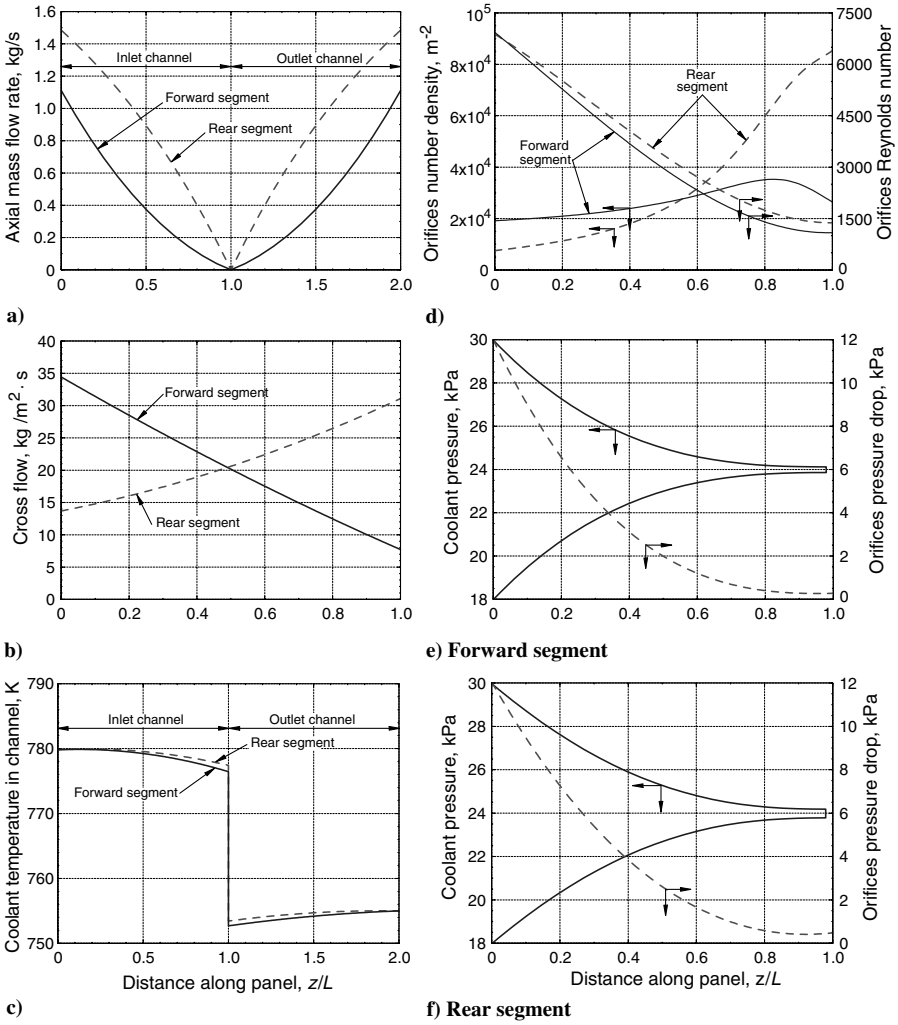


**Fig. 20 Lithium coolant conditions in the channels of the radiator segments.**

also increases (Fig. 21b). At a channel width ratio of about 0.3, the change in the length of the evaporator section of the heat pipes is nearly identical to that in the effective surface area of the heat pipes, and all heat pipes operate at nearly the same temperature (Fig. 21b). Thus, a width ratio of ~0.3 is a good choice for improving the thermal performance of the forward radiator segments.

The effects of $W_{back}/W_{in}$ on the specific power and heat rejection rate of the forward radiator segment are shown in Fig. 21c. The rate of heat rejection initially increases with increasing $W_{back}/W_{in}$, because the diameter of the heat pipes increases, decreasing both their thermal resistance and the width of the C–C fins. The heat rejection reaches an asymptote of 116.9 kW at a width ratio of ~0.60. Increasing the width ratio further does not increase the rate of heat rejection because the longer heat pipes operate at lower temperatures and transport less thermal power (Fig. 21b). This is because, again, the evaporator length of the longer heat pipes decreases with increasing $W_{back}/W_{in}$, increasing their thermal resistance. The mass of the forward segments of the radiator panels increases with increasing $W_{back}/W_{in}$ because the diameter of the heat pipes increases (Fig. 21a), and the height of the coolant channels increases to maintain a total pressure drop of 12 kPa.

The specific power of the forward segments increases quickly with increasing the rate of heat rejection initially, but peaks at a width ratio of 0.40 as the heat rejection reaches an asymptote while the radiator segment mass continues to increase (Fig. 21c). Based on these results, $W_{back}/W_{in} = 0.4$ is selected for the forward segment of the radiator panel, that is, the coolant channels are 10 cm wide at the entrance and 4 cm wide at the back end (Table 2). For this design, the specific power of the forward radiator segments is highest (2.157 kW/kg) and the rate of heat rejection is close (116.4 kW) to the peak value of 116.9 kW (Fig. 21c).

### Rear Radiator Segments

Results for the rear radiator segments with an average channel width of 8 cm and 144 Rb heat pipes are shown in Figs. 22a–22c. The shortest heat pipes are located at the entrance and the longest are at the back end of the coolant channels (Fig. 8b). The vapor flow area to ensure a vapor Mach number of 0.50 in the longest heat pipe of the exit-channel decreases with increasing $W_{back}/W_{in}$ because the evaporator section length increases. Similarly, the liquid annulus flow area in the longest heat pipe of the inlet-channel is selected to ensure that it operates at $\leq$ 50% of the capillary limit. The height of the coolant channels, and consequently the volume of lithium in the radiator segment, increase, but the width of the coolant channel at the inlet decreases as $W_{back}/W_{in}$ increases (Fig. 22b). The mass of the heat pipes decreases with increasing $W_{back}/W_{in}$, because their vapor flow area and dimensions decrease (Fig. 22a and 22b). The total mass of the radiator segment is the sum of the masses of the heat pipes, C–C fins, channel wall, and lithium coolant. It decreases rapidly with increasing $W_{back}/W_{in}$ to reach 68 kg at $W_{back}/W_{in} = 2.0$, as the diameter of the heat pipes reaches an asymptotic value (Fig. 22a), but the lithium coolant inventory in the channels keeps increasing (Fig. 22b).

As shown in Fig. 22c, the rate of heat rejection by the rear segments of the radiator panels decreases with increasing the channels width ratio because the diameter of the heat pipes decreases (Fig. 22a). Consequently, the specific power of the segment increases rapidly with increasing $W_{back}/W_{in}$, as the mass of the radiator

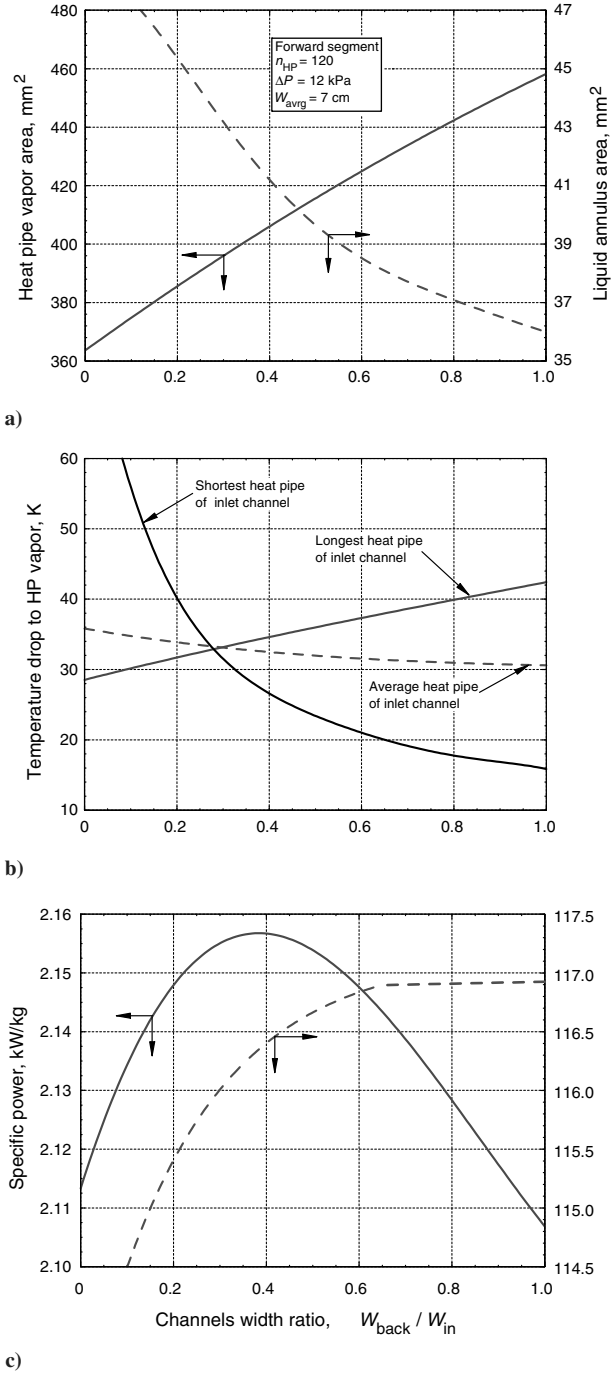


**Fig. 21 Effects of channel width ratio on performance of forward segment.**

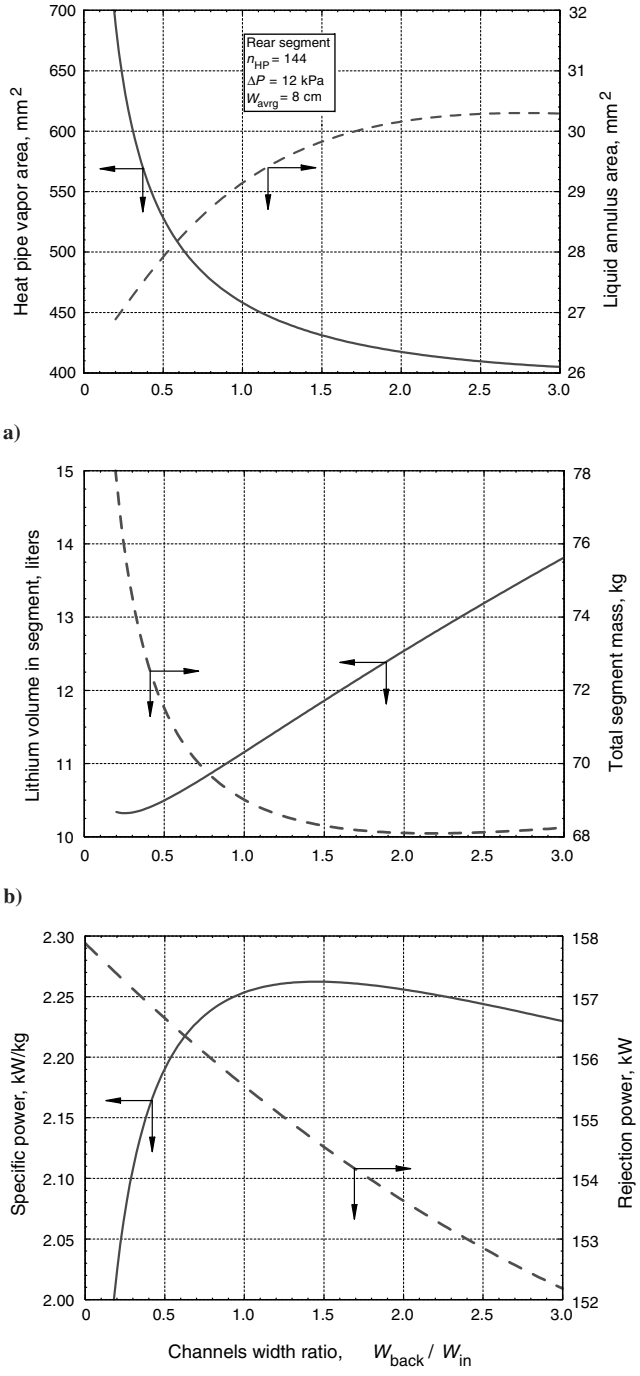


**Fig. 22 Effects of channel width ratio on performance of rear segment.**

segment decreases, reaching a peak near $W_{back}/W_{in} = 1.5$ (Fig. 22c). Beyond this point, the specific power of the rear radiator segments decreases slowly as the rate of heat rejection decreases while the mass of the segments remains essentially unchanged. Based on these results, a width ratio of 1.0 is selected for the rear radiator segments (Fig. 8b), for which the specific power is nearly optimum, 2.25 kW/kg, and both the segment mass (69.05 kg) and the lithium inventory (11.16 liters) are lowest (Fig. 22b).

Even though the channels height necessary to maintain a total pressure drop of 12 kPa decreases, the lithium volume in the rear segment increases (Fig. 23b) as the channels width increases. The mass of the heat pipes in the rear segment decreases with increasing the channels width, since their vapor flow area and dimensions decrease (Fig. 23a). As a result, the total mass of the segment decreases with increasing the width of the coolant channels, reaching a minimum at ∼8.5 cm, then increases with a further increase in the channels width because the masses of the lithium coolant and of the channels increase (Fig. 23b).

The calculated changes in the heat rejection and specific power of the rear radiator segments, as the channels width increases, are shown in Fig. 23c. The heat rejection rate increases with increasing the channels width because the heat pipes operate at higher temperature. Also, as the channel width increases and the diameter of the heat pipes decreases (Fig. 23a), the length of the C–C fins increases and their thermal efficiency decreases, slowing down the increase in the rate of heat rejection by the rear segments, which peaks at 155.6 kW each when the channels width is ∼8 cm (Fig. 23c). The specific power of the rear segments peaks at ∼2.25 kW/kg when the channels width is ∼8.5 cm (Fig. 23c). Based on these results, a channels width of 8 cm is selected for the rear segments of the radiator panels of the SCoRe-TE NRPS.

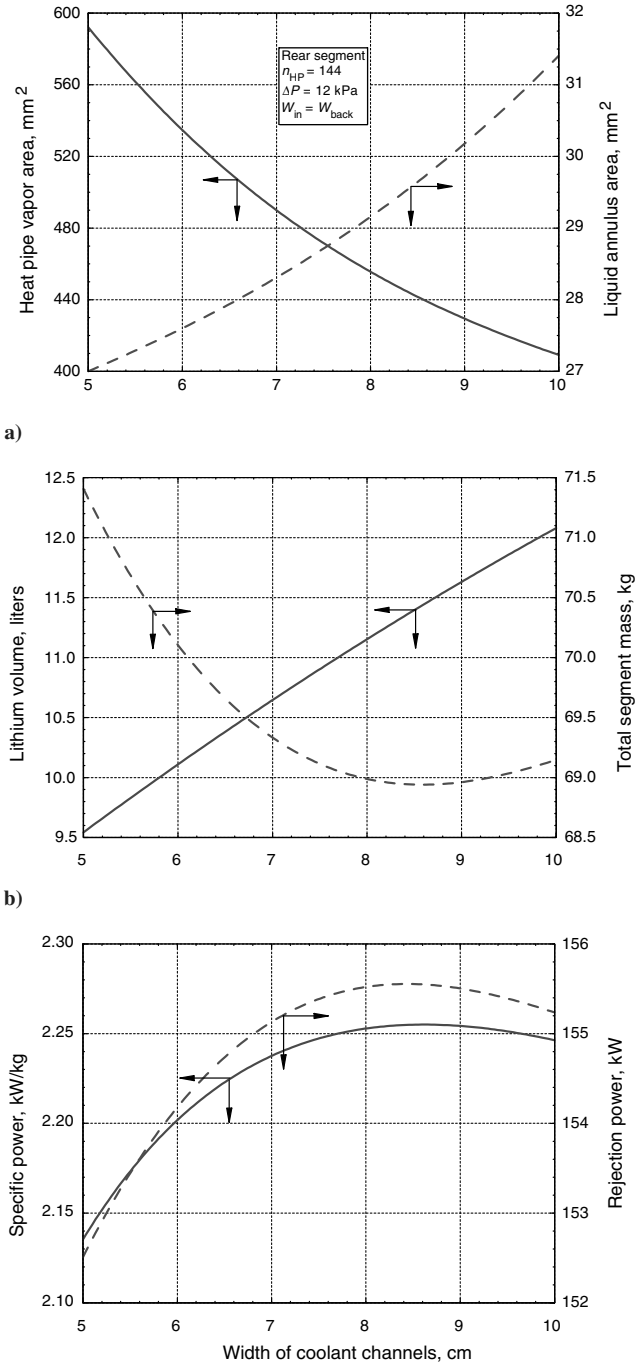


**Fig. 23 Effects of coolant channel width on rear segment performance.**

#### Effect of the Perforated Dividers

Table 2 compares the results for the radiator panels with (fourth and fifth columns) and without (second and third columns) perforated dividers. Bleeding the lithium flow in the coolant channels through the orifices in the perforated dividers reduces the cross-sectional areas of the inlet- and exit-channels for the same pressure losses of 12 kPa. The heights of the coolant channels in the forward and rear segments of the panel with perforated dividers are 0.822 and 1.177 cm, respectively, (fourth and fifth columns in Table 2), compared with 1.52 and 1.545 cm, respectively, without perforated dividers (second and third columns in Table 2).

The volume of the liquid lithium in the two rear deployable segments of each radiator panel with perforated dividers is $2 \times 11.16 = 22.32$ liters and increases to $2 \times 14.65 = 29.3$ liters in the segments without perforated dividers. Similarly, the lithium volume in the forward, fixed segment of each radiator panel with perforated dividers is 7.56 liters and increases to 14.0 liters in the same segment without perforated dividers. Thus, the larger cross-sectional flow areas of the coolant channels of the panel without perforated dividers increase the liquid lithium volume in the panel to 43.3 liters, compared with only 29.88 liters in the radiator panel with perforated dividers.

The heat rejection rate by each rear, deployable segment of the radiator panel without perforated dividers (157.2 $kW_{th}$) is slightly higher than that of the segment with perforated dividers (155.6 $kW_{th}$). Because the axial mass flow rate in the inlet- and exit-channels in the rear segment without perforated dividers is constant, the longest heat pipes operate at higher temperature than in the segment with perforated dividers. By contrast, in the rear segment with perforated dividers, the axial mass flow rate at the location of the longest heat pipes is relatively low, causing them to operate at a lower temperature and to transport and reject less thermal power. In the forward radiator segment, however, because the lithium mass flow rate at the longest heat pipes near the entrance and exit of the coolant channels is highest, the segment without perforated dividers rejects slightly less power (114.2 kW) than that with perforated dividers (116.4 kW). This is because the channels cross section flow area in the former is higher, and at the location of the longest heat pipes, the axial Reynolds number and Nusselt number are lower.

The dry mass of the segmented radiator without perforated dividers (1063 kg) is practically the same as that of the segmented radiator with perforated dividers (1060 kg), and the rate of heat rejection is almost the same, 2.571 and 2.566 $MW_{th}$, respectively. The major difference is that the liquid lithium inventory in the radiator without perforated dividers (259.8 liters and 134.3 kg) is significantly higher (by 80.5 liters and 41.5 kg) than that in the radiator with perforated dividers (179.3 liters and 92.8 kg). The larger lithium inventory in the radiator without perforated dividers also requires employing larger and heavier accumulators (Fig. 6) for the increase in lithium volume in the secondary loop ($\sim$7%), as it heats up from its fusion temperature (464 K) to nominal operating temperature ($\sim$800 K), adding to the total mass of the NRPS.

In the selected radiator for the SCoRe-TE NRPS, each forward segment with perforated dividers weighs 54.0 kg, has a dry specific mass of 5.43 kg/m$^2$, and a wet specific power of 2.16 kW/kg (see Table 2). Each rear segment weighs 69.05 kg, has a dry specific mass of 6.69 kg/m$^2$, and a wet specific power of 2.25 kW/kg (Table 2). For a total radiator heat rejection rate of 2.566 $MW_{th}$ each of the six radiator panels weighs 192.1 kg and rejects 427.6 $kW_{th}$. This radiator has an effective heat rejection area of 203 m$^2$, wet specific power of 2.23 $kW_{th}$/kg, average wet specific mass of 6.82 kg/m$^2$, and weighs 1153 kg, including $\sim$93 kg of lithium in the coolant channels.

## Summary and Conclusions

Four radiator configurations with the largest effective surface areas for NRPSs that could be stowed within the launch bay of the DELTA-IV Heavy vehicle are developed. These radiators have a 30 deg cone angle, a minor diameter of 1.08 m, and their effective and geometrical areas range from 69.1 to 350 m$^2$ and 56.76 to 274.38 m$^2$, respectively. The radiator with an effective surface area of 203 m$^2$ is selected for the SCoRe-TE NRPS for generating >100 kWe for 7–10 years. This radiator has six identical panels, each composed of a forward, fixed segment and two rear, deployable segments. The three segments of each panel are thermal-hydraulically coupled in parallel to reduce the lithium inventory in the coolant channels. The forward segment is 6.605-m-long, uses 120 Rb heat pipes, and has an effective surface area of 9.78 m$^2$, whereas each rear segment is 5.952-m-long, uses 144 Rb heat pipes, and has an effective area of 12.04 m$^2$. The longest and shortest heat pipes in the forward segment are 1.13 and 0.268-m-long, respectively, while those in the rear segments are 1.0 and 0.59-m-long, respectively.

Rubidium is selected as heat pipes working fluid because it results in a lower radiator mass. Its FOM is about 60% higher than that of

cesium, and its vapor pressure is higher than that of potassium in the temperature range of interest (700–760 K). The radiator heat pipes are D-shaped, for better thermal coupling to the lithium coolant channels, and operate nominally at or below 50% of the prevailing sonic or capillary limit. A heat pipe aspect ratio $\alpha = 0.5$ is selected, for which the cross section area and mass of the heat pipe are minimum. The capillary limit is most constraining in the longest heat pipe of the inlet-channel because it operates at higher temperature and transports more thermal power. By contrast, the highest vapor Mach number occurs in the longest heat pipe of the exit-channel, which runs cooler.

A thermal-hydraulic model is developed to investigate and optimize the performance of the heat pipes and the radiator segments. The height of the coolant channels is sized for a lithium coolant pressure drop of 12 kPa and inlet and exit coolant temperatures of 780 and 755 K, respectively. Investigated are the effects on the radiator's specific mass and liquid lithium inventory of 1) tapering the coolant channels in the forward and rear segments, 2) changing the width of the coolant channels (or the length of the heat pipes evaporator sections), and 3) using perforated dividers between the lithium inlet- and exit-channels. The orifices in the perforated dividers are 1.0 mm in diameter, and their number density is optimized to maintain almost uniform, but different, coolant temperatures in the inlet- and exit-channels. In the rear radiator segment, the longest heat pipes are located at the back end of the inlet and exit coolant channels, where the lithium axial flow rate and Nusselt number are lowest. As a result, the temperature drop through the lithium coolant and the channel wall is much larger under the longest heat pipes of the rear segment (31.7 K) than under the longest heat pipes of the forward segment (12.8 K). By contrast, in the forward segment, the axial flow rate and Nusselt number are highest at the location of the longest heat pipes. As a result, using perforated dividers and tapering the width of the coolant channels is extremely effective in reducing the cross-sectional areas of the channels, the lithium inventory, and the specific mass of the forward segment, but has a less pronounced effect in the rear segment.

Based on the optimization results, the lithium coolant channels in the forward segments are 0.822 cm high and their width is tapered linearly between 10 cm at the inlet to 4 cm at the back end of the channel. For this design, the segment's specific power is highest (2.16 kW/kg) and the rate of heat rejection is near (116.4 kW) the peak value of 116.9 kW. The coolant channels of the rear segment are rectangular with a constant width of 8 cm and height of 1.177 cm, for which the rate of heat rejection is maximum (155.6 kW), and both the segment mass (69.05 kg) and the lithium inventory (11.16 liters) are lowest. The optimized radiator for the SCoRe-TE NRPS has an average, wet specific mass of 6.82 $kg/m^2$, and lithium coolant inventory of 179.3 liters. With segmented panels without perforated dividers, these values are 7.09 $kg/m^2$ and 260 liters, respectively.

## Acknowledgment

This work is funded by the University of New Mexico's Institute for Space and Nuclear Power Studies.

## References

[1] El-Genk, M. S., "Energy Conversion Technologies for Advanced Radioisotope and Nuclear Reactor Power Systems for Future Exploration," *2002 Proceedings, Twenty-First International Conference on Thermoelectrics (ICT)*, Inst. of Electrical and Electronics Engineers, Piscataway, NJ, 2002, pp. 375–380.

[2] El-Genk, M. S., and Tournier, J.-M., "SAIRS—Scalable AMTEC Integrated Reactor Space Power System," *Progress in Nuclear Energy*, Vol. 45, No. 1, 2004, pp. 25–69.

[3] Bevard, B. B., and Yoder, G. L., "Technology Development Program for an Advanced Potassium Rankine Power Conversion System Compatible with Several Space Reactor Designs," *Proceedings of the Space Technology and Applications International Forum (STAIF-2003)*, AIP-CP-654, edited by M. S. El-Genk, American Inst. of Physics, Melville, NY, 2003, pp. 629–634.

[4] Lipinski, R. J., Lenard, R. X., Wright, S. A., Houts, M. G., Patton, B., and Poston, D., "Fission-Based Electric Propulsion for Interstellar Precursor Missions," *Proceedings of the Space Technology and Applications International Forum (STAIF-2000)*, AIP-CP-504, edited by M. S. El-Genk, American Inst. of Physics, Melville, NY, 2000, pp. 974–983.

[5] Barrett, M. J., and Reid, B. M., "System Mass Variation and Entropy Generation in 100 kWe Closed-Brayton-Cycle Space Power Systems," *Proceedings of the Space Technology and Applications International Forum (STAIF-2004)*, AIP-CP-699, edited by M. S. El-Genk, American Inst. of Physics, Melville, NY, 2004, pp. 445–452.

[6] Schmitz, P. C., Schreiber, J. G., and Penswick, B., "Feasibility Study of a Nuclear-Stirling Power Plant for the Jupiter Icy Moons Orbiter," *Proceedings of the Space Technology and Applications International Forum (STAIF-2005)*, AIP-CP-746, edited by M. S. El-Genk, American Inst. of Physics, Melville, NY, 2005, pp. 738–749.

[7] Tournier, J.-M., and El-Genk, M. S., "Radiator Heat Pipes with Carbon–Carbon Fins and Armor for Space Nuclear Reactor Power Systems," *Proceedings of the Space Technology and Applications International Forum (STAIF-2005)*, AIP-CP-746, edited by M. S. El-Genk, American Inst. of Physics, Melville, NY, 2005, pp. 935–945.

[8] El-Genk, M. S., and Tournier, J.-M., "Startup and Load-Following Transients of a Thermoelectric Space Reactor System with No Single Point Failure," *Proceedings of the 3rd International Energy Conversion Engineering Conference (IECEC-2005)*, AIAA Paper No. 2005-5715, 2005.

[9] El-Genk, M. S., and Tournier, J.-M., "DynMo: Dynamic Simulation Model for Space Reactor Power Systems," *Proceedings of the Space Technology and Applications International Forum (STAIF-2005)*, AIP-CP-746, edited by M. S. El-Genk, American Insti. of Physics, Melville, NY, 2005, pp. 1005–1020.

[10] Boeing Launch Services, "DELTA-IV Technical Summary," http://www.boeing.com/defense-space/space/delta/product-card/pc_d4_tech_print.pdf [cited 15 April 2005].

[11] Rovang, R. D., Hunt, M. E., Dirling, R. B., Jr., and Holzl, R. A., "SP-100 High-Temperature Advanced Radiator Development," *Proceedings of the 8th Symposium on Space Nuclear Power Systems, CONF-910116*, Vol. 2, edited by M. S. El-Genk, and M. D. Hoover, American Inst. of Physics, New York, NY, 1991, pp. 702–707.

[12] El-Genk, M. S., Hatton, S., Fox, C., and Tournier, J.-M., "SCoRe—Concepts of Liquid Metal Cooled Space Reactors for Avoidance of Single-Point Failure," *Proceedings of the Space Technology and Applications International Forum (STAIF-2005)*, AIP-CP-746, edited by M. S. El-Genk, American Inst. of Physics, Melville, NY, 2005, pp. 473–484.

[13] El-Genk, M. S., Saber, H. H., and Caillat, T., "A Performance Comparison of SiGe and Skutterudite Based Segmented Thermoelectric Devices," *Proceedings of the Space Technology and Applications International Forum (STAIF-2002)*, AIP-CP-608, edited by M. S. El-Genk, American Inst. of Physics, Melville, NY, 2002, pp. 1007–1015.

[14] Truscello, V. C., and Rutger, L. L., "The SP-100 Power System," *Proceedings of the 9th Symposium on Space Nuclear Power Systems*, AIP-CP-246, edited by M. S. El-Genk, and M. D. Hoover, American Inst. of Physics, Melville, NY, 1992, pp. 1–23.

[15] Rider, W. J., and El-Genk, M. S., "Transient and Parametric Analyses of SP-100 Type Systems," *Space Nuclear Power Systems 1989*, edited by M. S. El-Genk, and M. D. Hoover, Vol. 11,Orbit , Malabar, FL, 1992, Chap. 41, pp. 419–434.

[16] Tournier, J.-M., and El-Genk, M. S., "A Vapor Flow Model for Analysis of Liquid-Metal Heat Pipes Startup from a Frozen State," *International Journal of Heat and Mass Transfer*, Vol. 39, No. 18, 1996, pp. 3767–3780.

[17] Bird, R. B., Stewart, W. E., and Lightfoot, E. N., *Transport Phenomena*, Wiley, New York, NY, 1960, Section 9.7, pp. 288–291.

[18] Idelchik, I. E., *Handbook of Hydraulic Resistance*, 2nd ed., revised and augmented, edited by E. Fried, Hemisphere, Washington, D.C., 1986, Chap. 4, pp. 151–159.

[19] MatLab, "MATLAB® 7.0.1," http://www.mathworks.com/products/matlab [cited 15 Sept. 2004].

[20] Simulink, "SIMULINK® 6.1," http://www.mathworks.com/products/simulink [cited 15 September 2004].

G. Spanjers
*Associate Editor*